Sensors & Actuators: B. Chemical 417 (2024) 136150

Contents lists available at ScienceDirect

Sensors and Actuators: B. Chemical

journal homepage: www.elsevier.com/locate/snb

Multimodal HOCl-responsive MEH-PPV nanoparticles for anti-inflammatory imaging and therapy

Eva Villar-Alvarez [a], Sara Parron-Onate [a], Olga Wienskowska [a], Aleix Carrascull-Marín [a], Christian Bellacanzone [a], Julia Lorenzo [b,c,d], Daniel Ruiz-Molina [a,*], Claudio Roscini [a,*]

[a] Catalan Institute of Nanoscience and Nanotechnology (ICN2), CSIC and BIST, Campus UAB, Bellaterra, Barcelona 08193, Spain
[b] Institut de Biotecnologia i de Biomedicina, r, Universitat Autònoma de Barcelona, Cerdanyola del Vallès 08193, Spain
[c] Departament de Bioquímica i Biologia Molecular, Universitat Autònoma de Barcelona, Cerdanyola del Vallès 08193, Spain
[d] Centro de Investigación Biomédica en Red: Bioingeniería, Biomateriales y Nanomedicina, Cerdanyola del Vallès 08193, Spain

ARTICLE INFO

Keywords:
Fluorescence probe
Hypochlorous acid
Inflammatory disease
MEH-PPV
Quercetin
Theranostic

ABSTRACT

Inflammatory disorders often correlate with an unusually high intracellular production of hypochlorous acid (HOCl). Therefore, its rapid, sensitive, and specific detection is crucial for an early diagnosis and treatment evaluation. While nanoparticles for detection have already been reported, multimodal nanoparticles that simultaneously detect and eliminate reactive oxygen species (including the excess of HOCl) are scarce despite their interest. Herein, we developed highly selective fluorescent nanoparticles using the copolymer poly(2-methoxy-5-(2-ethylhexyloxy)-1, 4-phenylenevinylene) (MEH-PPV), with (MEH@CS) and without a chitosan coating (MEH). The conjugated polymer is oxidized in the presence of HOCl, exhibiting a rapid (in less than 30 s) and sensitive fluorescence turn-off response with a log-log linear HOCl relationship within dynamic ranges of ≈ 0.784–83 μM and ≈ 0.384–55 μM for MEH and MEH@CS NPs, respectively, allowing to monitor basal HOCl levels within the standard physiological concentration range (5 – 25 μM) and its differentiation from over-production. Moreover, the nanoparticles can encapsulate and release quercetin (a powerful natural scavenger for HOCl), leading not only to monitoring but also to a reduction in pro-inflammatory cytokines of inflammation-stimulated macrophage cells.

1. Introduction

Hypochlorous acid (HOCl), one of the most significant reactive oxygen species (ROS) in the human body, is generated through the conversion of hydrogen peroxide (H_2O_2) and Cl^- anions of the cellular fluid, catalyzed by the myeloperoxidase (MPO) enzyme present in the mitochondria [1–3]. HOCl is involved in immune reactions that help fight invasive bacteria and kill pathogens [1–3] and it also contributes to the regulation of the crucial physiological processes such as cell proliferation and apoptosis [3,4]. However, intracellular levels of HOCl over specific thresholds (reaching values as high as 340 μM), relate to various inflammatory diseases, such as asthma, rheumatoid arthritis, atherosclerosis and neurodegenerative disorders like Parkinsonś and Alzheimer's disease, and can induce DNA fragmentation and protein oxidation through oxidative stress [1,3–7]. Therefore, the development of effective methods for the rapid, sensitive, and specific recognition of endogenous HOCl is crucial in the prevention of inflammatory diseases [4–7]. With this aim, several bioanalytical HOCl-detection techniques have been developed in the past decades, such as colorimetric, bioluminescent, luminescent, electrochemical, and chromatographic methods [6,7]. Among them, optical approaches have become popular. Numerous molecular fluorescent probes have been reported [8–20] revealing their non-invasive nature, high sensitivity with spatial resolution, real-time detection (time response as fast as 40 s), far-red/near infrared emitting properties, and good biocompatibility [5,7–10]. However, most of them still suffer from limited chemical and colloidal stability, lack any mitochondrial-targeting ability, exhibit slow response and low fluorescence quantum yield and have restricted emission wavelengths, making it difficult to discriminate from autofluorescence [5,7,21].

To overcome this challenge, nanostructuration of the dyes has emerged as a versatile alternative [22]. Representative examples include self-calibrating nanopolymers with dual targeting [23], a pyrene/pyridyl-based ultrafine reactive fluorescent turn-off nanoprobe

* Corresponding authors.
E-mail addresses: dani.ruiz@icn2.cat (D. Ruiz-Molina), claudio.roscini@icn2.cat (C. Roscini).

https://doi.org/10.1016/j.snb.2024.136150
Received 23 December 2023; Received in revised form 5 May 2024; Accepted 15 June 2024
Available online 18 June 2024

[24], fluorescent polymeric nanoparticles with single-wavelength excitation [25], a nanoflare-based DNA sensor assembled with a gold nanoparticle [26], turn-off naphthalimide-functionalized fluorescent silica nanoparticles [27], or a nanoprecipitated dual-functional (HOCl and Cl^-) fluorescent nanosensor [28]. However, fewer examples of multimodal nanoparticles that simultaneously detect and release free-radical scavengers or antioxidants have been reported, in spite of their interest. Yan et al [29] developed a P-selectin targeting PLGA-based nanocarrier doped with two lipophilic dyes and co-delivering betulinic acid and resveratrol drugs, known ROS scavengers. In this case, ROS imaging was achieved by fluorescence resonance energy transfer BRET-FRET effect injecting non-linked luminol to the NPs. Ma et al. [30], successfully synthesized theranostic NPs linking, a two-photon AIE fluorophore and the antioxidant drug prednisolone via a ROS-responsive bond, but the detection seems to be unspecific for an oxidant molecule. Liu and co-workers [31], also reported a HOCl-activated fluorescent nanoplatform based on Au NPs coated with a sensitive HOCl probe and the redox drug methylene blue on its surface, showing HOCl concentration-dependent photoacoustic signal intensity for quantification specifically for cancer therapy. Wei et al [32]. developed a highly sensitive probe conjugated with an antioxidant prodrug, that easily integrates into a single structure HOCl detection in NIR emission and therapy through the selective breaking of amino and carboxyl groups. All in all, these few examples so far reported confirm the possibility to combine both monitoring and down-regulation of ROS levels (including the excess of HOCl). However, this research area is still at early development stages with further developments needed, specially achieving multimodal and sensitive nanoplatforms with fast detection responses while still autoregulating ROS extent.

Here we demonstrate that nanoparticles (NPs) of the poly(2-methoxy-5-(2-ethylhexyloxy)-1,4-phenylenevinylene) (MEH-PPV) polymer are promising candidate for this. Indeed, HOCl-induced oxidation shortens the inter/intramolecular conjugation polymer length, not only modifying its emission and absorption properties [33, 34], but simultaneously releasing anti-inflammatory drugs. The nanoparticle fabrication method was precipitation/solvent diffusion method [35–39], and the encapsulated HOCl scavenger, quercetin (QCT) (see Scheme 1) [40–45]. It is a natural flavonoid showing excellent anti-inflammatory and antioxidant properties in experimental models of atherosclerosis, diabetes, and hypertension [41,46]. To further enhance cellular uptake, the nanoparticles were additionally coated with the polysaccharide chitosan (CS) [45–49]. The activity of the resulting QCT-MEH@CS nanoplatform was studied on HeLa cancer cells and RAW264.7 murine macrophages, a commonly used *in vitro model* for *inflammation studies,* stimulated with phorbol myristate acetate (PMA) and lipopolysaccharide (LPS) to produce endogenous HOCl. Analysis of cell viability, fluorescence and the inhibition of the pro-inflammatory cytokines interleukin-6 (IL-6) and tumor necrosis factor-alpha (TNF-α) [50–54], showed excellent results confirming the validity of our approach (non-coated MEH NPs were also analyzed and studied for comparison purposes).

2. Materials and methods

2.1. Materials

Poly[2-methoxy-5-(ethylhexyloxy)-1,4-phenylenevinylene] (MEH-PPV) (MW 40,000–70,000), chitosan oligosaccharide lactate (MW 5000), potassium phosphate dibasic and monobasic anhydrous, iron (II) perchlorate, potassium superoxide (KO_2), sodium sulfite (Na_2SO_3), quercetin (QCT), lipopolysaccharides from Escherichia coli O55:B5 (LPS), phorbol 12-myristate 13-acetate (PMA), and crystal violet were acquired from Sigma-Aldrich. Sodium hypochlorite (NaOCl, 11–15 %) was purchased from Alfa Aesar. Tetrahydrofuran (THF) anhydrous, acetic acid (glacial 99.5 %), hydrochloric acid (HCl, 37 %) and dimethyl sulfoxide (DMSO) were acquired from Scharlau. Hydrogen peroxide (H_2O_2, 35 %) was obtained from Fluka. Nylon and polyethersulfone (PES) filters (0.22 μm) were purchased in Branchia and Fisher brand, respectively. Fetal Bovine Serum (FBS), Dulbecco's modified Eagle's medium (DMEM), Minimum Essential Medium-α GlutaMAX no nucleosides (MEM-α), Trypsin-EDTA (0.25 %), and Phosphate buffer saline 1X (PBS) were from Gibco Life technologies. The BD™ CBA Mouse Inflammation Kit was purchased from BD Biosciences. Milli-Q water was used in all the experiments.

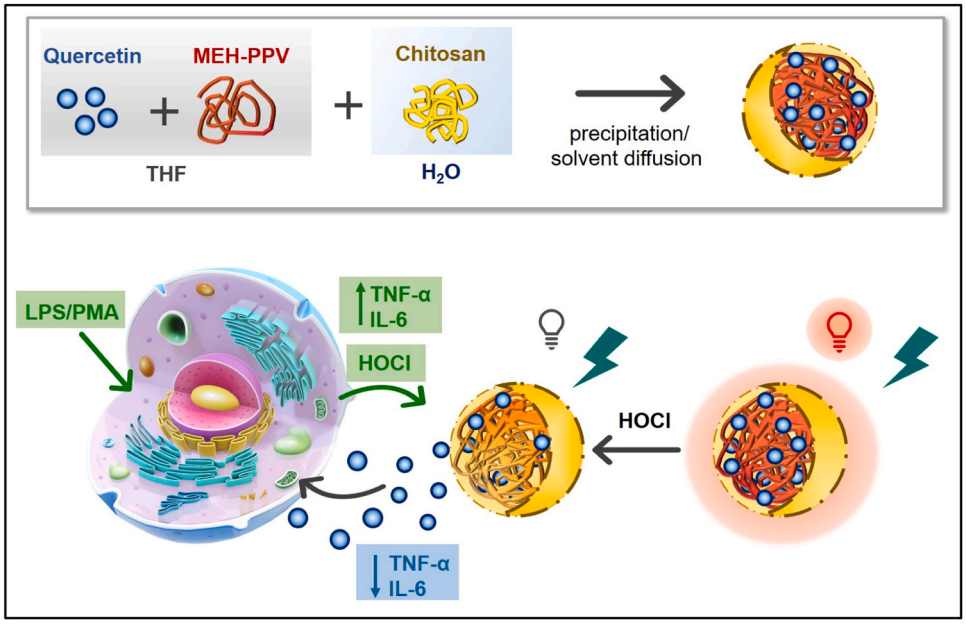

Scheme 1. Graphic representation of QCT-MEH@CS NP preparation and the mechanism behind their multimodal capabilities for detecting and treating inflammation. The preparation process of QCT-MEH@CS nanoparticles is the precipitation/solvent diffusion method (top). NPs' fluorescence turn-off response in presence of endogenous HOCl generated by LPS/PMA stimulation while the released QCT down-regulates HOCl concentration, as well as the pro-inflammatory cytokines IL-6 and TNF-α (bottom).

2.2. Synthesis of MEH-PPV-based NPs

2.2.1. Synthesis of MEH NPs

MEH nanoparticles (NPs) were obtained by precipitation through the solvent-diffusion method[39]. Firstly, 1.5 mg of MEH-PPV (Scheme S1A) was dissolved in 3 mL of THF (0.5 mg mL^{-1}). The solution was sonicated in an ultrasound bath for 10 min to completely dissolve the polymer. 1 mL of the MEH-PPV solution was quickly added to 4 mL of water upon vigorous stirring (1400 rpm). The stirring was immediately stopped after the addition. The as-formed NPs were stirred (700 rpm) at room temperature (RT) for 4 h in order to evaporate the organic solvent. After that, NPs were filtered with a 0.22 μm PES filter. MEH NPs (and the next synthesized MEH@CS and QCT-MEH@CS NPs suspensions) were stored in a refrigerator at 4°C and covered with Al foil during all experiments to prevent the possible light-induced degradation of the copolymer.

2.2.2. Synthesis of MEH@CS NPs

Chitosan (CS)-coated MEH NPs (MEH@CS NPs) were obtained following the same protocol as for MEH NPs, except the aqueous phase, which consisted of a 7 mL chitosan (CS) (Scheme S1B) solution (14.3 μg mL^{-1}). Preformed CS solution (1 mg mL^{-1}) was prepared in acetic acid (1 % v/v) and stirred at 300 rpm for 4 h at RT. After the synthesis, NPs were filtered with a 0.22 μm Nylon filter.

2.2.3. Synthesis of QCT-MEH NPs and QCT-MEH@CS NPs

The synthesis of QCT-containing nanoparticles (QCT-MEH NPs and QCT-MEH@CS NPs) loading different concentration of QCT followed the same protocols as for MEH NPs and MEH@CS NPs, respectively, with the following variations (Scheme S1C): first, 0.5 mg of MEH-PPV was mixed with the corresponding volume of a preformed THF quercetin stock solution. THF was added to that mixture until it reached 3 mL. Then, the solutions were sonicated for 10 min to homogenize. Several MEH-PPV:QCT molar ratios between 1:18 and 1:36 were used to form the NPs. After that, the corresponding solution was quickly added to 4 mL of Milli-Q water (if QCT-MEH NPs were desired) or to the chitosan aqueous phase (for the QCT-MEH@CS NPs).

2.2.4. Preparation of oxidizing agents

Hydrogen peroxide (H_2O_2) and hydrochloric acid (HCl) solutions were prepared by diluting the compounds directly in MilliQ water until the desired concentration of the stock solution was reached. Hypochlorous acid (HOCl) and bisulfite ion (HSO_3^-) solutions were obtained by diluting sodium hypochlorite (NaOCl) and sodium sulfite (Na_2SO_3), respectively, in MilliQ water, following the procedure described before [28]. Superoxide anion ($\bullet O2^-$) was accomplished by dissolving potassium superoxide (KO_2) in dimethyl sulfoxide (DMSO) at 1 mM[28]. Finally, hydroxyl radical (•OH) was produced by combining iron (II) perchlorate (1 mM) with H_2O_2 (3 mM)[28]. To evaluate selectivity towards HClO by fluorescence spectroscopy, equal volumes of freshly prepared oxidizing agents and NPs (in phosphate buffer pH 5.7) at twice the desired concentration were mixed, resulting in final concentrations of 23 μg mL^{-1} for NPs, 100 μM for H_2O_2, and 15 μM for HOCl, HCl, •OH, $\bullet O2^-$ and HSO_3^-. All measurements were performed before and after 1 h of incubation.

2.3. NPs characterization

2.3.1. Dynamic light scattering (DLS) and Z-potential (ZP) measurements

Size and ZP measurements were performed using the Malvern Z-sizer nano-zs with a 173° scatter angle. NPs were diluted in water at 25 ºC, except when another temperature is indicated. A disposable folded capillary cell was used for both ZP and DLS measurements. To ensure accuracy, average values were obtained from 3 cycles (both size and ZP).

2.3.2. Scanning and transmission electron microscopies

SEM images were acquired using the FEI Quanta 650 FEG microscope. Sample suspensions (100 – 150 μL) were deposited on metal stubs covered with Al tape, air-evaporated overnight (O/N), and coated with a 5 nm layer of Pt. TEM (and STEM) images were recorded using a JEOL 1400 TEM microscope operated at 120 kV. A droplet of NPs suspension (10 – 50 μL) was placed and dried onto Ted-Pella carbon-coated copper grids.

2.3.3. UV-Vis and fluorescence spectroscopies

Absorption spectra of NPs were recorded in transmission mode using the Agilent Cary 60 spectrophotometer, employing a 1×1 cm quartz cuvette. Depending on the sample solvent, water, THF or phosphate buffer saline (PBS) were used as blanks. Fluorescence emission spectra of NPs were measured by means of a PTI QuantaMaster 300 phosphorescence/fluorescence spectrophotometer (Horiba Ltd.), using a 1×1 cm quartz fluorescence cuvette. All emission spectra were obtained using a pulsed Xenon lamp, to reduce the risk of NPs' photodegradation due to the minimized irradiation time. The excitation wavelength was fixed at the absorption maximum (λ_{exc} = 490 nm). The dilution effect was corrected for the final emission spectra when applied. Fluorescence intensity of 9, 10-diphenylanthracene (DPA), was used as a reference standard for experiments conducted over several days[55]. Absolute quantum yield was examined using a C9920–02 G absolute quantum yield spectrometer (Hamamatsu), equipped with an integrating sphere to capture all light emitted from the sample without requiring a reference. The amount of absorbed photons was determined from the scattering peaks at the excitation wavelength of the incident light, given by the blank (cuvette-filled solvent) and sample.

2.3.4. Kinetics experiment

A quartz glass fluorescence cuvette was filled with a solution containing 23 μg mL^{-1} in MilliQ water of the corresponding MEH-PPV NPs, followed by the addition of 10 μM of HOCl. The fluorescence intensity of the solution was recorded as a function of time using a C9920–02 G absolute quantum yield spectrometer (Hamamatsu), equipped with an integrating sphere to capture all light emitted from the sample. The measurements were taken over a period of 2 min (λ_{exc} = 490 nm). The response time at 90 % ($t_{90\,\%}$), which is the time required by the NPs to reach 10 % of intensity difference between the emission at t_0 (I_0, before exposure to HOCl) and the fluorescence at steady state (I_{steady}), when it does not change over time, was determined as follows: first the loss rate of fluorescence was calculated using the formula: Integrated PL. Loss Rate = $[I(t) - I_{steady}]/[I_0 - I_{steady}]$. Then the resulting curve was fitted to a non-linear curve (biexponential) and the time at a fluorescence loss of 0.1 was interpolated to estimate a value for $t_{90\,\%}$.

2.3.5. Quantitative analysis of QCT in QCT-MEH@CS NPs

To determine the mass of QCT loaded in the QCT-MEH@CS NPs, the following procedure was used. After THF evaporation in the last step of the synthesis, the supernatant of QCT-MEH@CS and MEH@CS NPs was removed using an UF cross-flow filter (mPES 750 kDa, Spectrum® MicroKross). Then, concentrated NPs were diluted in water. QCT-MEH@CS and MEH@CS NPs were lyophilized for 1 day, and the same amount of NPs were subsequently added to 3 mL of THF, followed by 15 min of sonication to disrupt the NPs and redissolve the drug and/or polymers. The amount of encapsulated QCT was determined as the difference in absorption between the THF solutions of the redissolved QCT-MEH@CS and MEH@CS NPs (since absorption is additive in the linear range below 1), measured by UV-Vis at 372 nm [42,46]. The concentration of the QCT was determined from a calibration curve using the Lambert-Beer's law (see Fig. S10C). Each molar ratio was measured in triplicate from different batches and the final results were averaged. To determine the encapsulation efficiency (EE) and the loading capacity (LC) of the obtained nanocarriers, the following expressions were used [49]: EE (%) = [QCT encapsulated (g)] x 100 / [Total QCT fed (g)], LC

(%) = [QCT encapsulated (g)] x 100 / [QCT encapsulated (g) + MEH-PPV (g)].

2.4. Biological characterization

2.4.1. Cell culture

RAW264.7 murine macrophage cells (ATCC) were cultured in Dulbecco's Modified Eagle Medium (DMEM) supplemented with 10 % (v/v) fetal bovine serum (FBS) in an atmosphere of 10 % CO_2 at 37 ºC. Human cervical adenocarcinoma cells HeLa (ATTC) were cultured in Minimum Essential Medium-α GlutaMAX with no nucleosides (MEM-α) supplemented with 10 % (v/v) FBS in an atmosphere of 5 % CO_2 at 37 ºC. In all experiments, cells were grown to 80–90 % confluence before trypsinization and subjected to no more than 30 cell passages.

2.4.2. Cytotoxicity assay

To evaluate the toxicity of NPs, cells were seeded (5 000 cells per well) in a 96-well plate and allowed to adhere for 24 h. A range of concentrations from 0 to 100 μg mL^{-1} of the corresponding MEH and MEH@CS NPs, as well as 30 μg mL^{-1} of QCT-MEH@CS NPs obtained from different MEH-PPV:QCT ratios, were added in triplicate. Cell survival was determined after 24 and 48 h of incubation using the crystal violet viability assay protocol[56]. This assay was chosen to ensure that the dye absorbance (λ_{max}^{abs} = 590 nm) was not influenced by the NPs absorption (λ_{max}^{abs} = 490 nm), as observed in other cytotoxicity tests (MTT, CCK8). Absorption was measured using the SpectraMaxR iD3 multi-mode microplate reader (Molecular Devices) and compared to control wells, containing cells without NPs. Background signals were eliminated by subtracting the average signal from wells without cells. The average absorption of NP-free cells was set to 100 %. Each experiment was conducted independently three times to ensure accuracy and reproducibility. The following equation for cell survival rate (SR) was used: SR (%) = (OD_treated_cells – OD_blank) × 100 / (OD_control_cells – OD_blank), where OD is the optical density at 590 nm.

2.4.3. Confocal and epi-fluorescence microscopy

Bioimaging fluorescence confocal microscopy (TCS SP5, Leica) was used to visualize qualitatively the internalization of the MEH-PPV NPs (MEH and MEH@CS NPs). For confocal images, 80 000 cells/well were seeded on Mattek glass-bottom microwell dishes (35 mm dishes, 14 mm glass microwell diameter, No. 1.5 coverglass of 0.16 mm thickness). After 24 h, MEH and MEH@CS NPs (30 μg mL^{-1}) were added and incubated for an additional 24 h. Subsequently, microwells were washed twice with pre-warmed PBS to remove non-internalized NPs. Cell membranes were stained with Cell Mask deep red dye, and mitochondria with Biotracker 400 Blue (Sigma-Aldrich).

NPs internalization was also followed by bright field (BF) and epi-fluorescence (EF) microscopy (Nikon eclipse Ts2R microscope). For that, 20,000 cells were seeded in 24-well plates and incubated for 24 h for cell adhesion. MEH and MEH@CS NPs (30 μg mL^{-1}) were incubated for 6 and 24 hours. Afterward, wells were washed twice with pre-warmed PBS to remove non-internalized NPs and, subsequently, the medium without red phenol was added to visualize live cells. EF images were taken with an excitation wavelength of 470/40 nm (green channel). BF and EF images were merged, using the open-source graphics editor FIJI (ImageJ). For colocalization experiments, the same protocol was followed except for incubation with the mitochondrial tracker (MitoTracker red, ThermoFisher-Invitrogen) after PBS washes, visualized with an excitation wavelength of 525/50 nm (red channel). JaCop and colocalization finder plugging for FIJI software were used to calculate Pearson's coefficient.

2.4.4. Flow cytometry

In order to quantify the MEH-PPV NPs internalization, a flow cytometry assay was carried out using the Cytoflex flow cytometer (Beckman Coulter) recording 10,000 events (applying the detector filter in the phycoerythrin (PE) channel, 585/42 nm) after excitation with a blue laser (488 nm) and analyzing them with CytExpert software. For this assay, 100,000 cells/well were seeded in a 12-well plate and incubated for 24 h for cell adhesion. Subsequently, the culture medium was replaced with NPs (30 μg mL^{-1} in cell culture medium), and the cells were incubated for the desired period of time for NPs internalization. After that, cells were washed twice with PBS to remove non-internalized NPs, trypsinized and collected in Eppendorf tubes. Next, samples were centrifuged and the pellet was resuspended in 0.5 mL of medium without phenol red. Cells incubated without NPs were used as reference. The experiment was conducted independently three times to ensure accuracy and reproducibility.

2.4.5. HOCl in vitro detection and inhibition

To examine the NPs responsiveness to HOCl *in vitro*, cells were stimulated with LPS and PMA. Briefly, 50,000 cells/well were seeded in a 12-well plate. After 24 h, MEH, MEH@CS and QCT-MEH@CS NPs (30 μg mL^{-1}), were added to the corresponding wells, resuspended in cell culture medium and incubated for 24 h. Afterward, cells were washed twice with PBS, to remove non-internalized NPs. To stimulate the HOCl production, the corresponding concentration of LPS in culture medium was added to the corresponding wells. After 6 h of incubation, PMA (usually 1 μg mL^{-1}, unless otherwise indicated) was added directly and incubated for 1 h. Subsequently, cells were washed twice with PBS, trypsinized and collected in Eppendorf tubes. Samples were centrifuged and resuspended in 300 μL of PBS. The samples were measured using the same conditions as in the uptake assay using the Cytoflex flow cytometer (Beckman Coulter). Untreated cells and LPS/PMA-stimulated cells were used as controls. Each concentration was tested in triplicate and conducted independently three times to ensure accuracy and reproducibility.

2.4.6. Determination of IL-6 and TNF-α levels by ELISA

Levels of tumor necrosis factor-alpha (TNF-α) and interleukine-6 (IL-6) cytokines in each sample were determined using a commercially available CBA mouse inflammation ELISA kit from BD Biosciences according to the manufacturer's instructions. Briefly, 50,000 cells/well of RAW264.7 macrophages were cultured in a 12-well plate for 24 h. Afterwards, QCT-MEH@CS NPs (30 μg mL^{-1}) with different MEH-PPV: QCT ratios were added, resuspended in cell culture medium, and incubated for 24 h. After washing the cells twice with PBS to remove non-internalized NPs, the cells were stimulated with LPS (5 μg mL^{-1}). After 6 h of incubation, PMA (1 μg mL^{-1}) was directly added and incubated for 1 h. Cell culture supernatants were collected and immediately quantified using ELISA kits according to the manufacturer's instructions using a FACSCalibur flow cytometer (Becton Dickinson). Untreated cells, LPS/PMA-stimulated cells and MEH@CS treated cells were controls.

2.4.7. Statistical Analysis

OriginPro (Version 2022, OriginLab Corporation, Northampton, MA, USA) was used for statistical analysis/graphing, except for IC50 values that were determined by a four-parameter nonlinear logistic regression model using GraphPad Prism (Version 10.2, GraphPad Software Inc., Boston, MA, USA). The NPs fluorescence intensity was obtained from the integration of the emission spectra and expressed as the mean ± SD of three independent experiments ($n = 3$), except for QCT encapsulation ($n = 5$). All statistical analyses were analyzed with a two-tailed Student's t-test, with a p-value less than 0.05 considered statistically significant.

3. Results and discussion

3.1. Synthesis and physicochemical characterization

MEH-PPV-based NPs (i.e., MEH and MEH@CS NPs) were prepared by the precipitation/solvent diffusion method [37–39,57] and its

surface modified with CS [46–49] combining the solvent diffusion method with the Layer-by-Layer (LbL) technique [57]. Briefly, a solution of the fluorescent hydrophobic polymer MEH-PPV dissolved in a volatile solvent, miscible in water (THF), was quickly injected into Milli-Q water under vigorous stirring. The organic solvent diffuses rapidly to the aqueous phase, inducing the precipitation of the polymer and forming the nanoparticles (MEH NPs). Simultaneously, if the cationic polymer CS was previously dissolved in the aqueous phase, it adsorbs onto the NPs surface through Van der Waals but mainly via electrostatic interactions with the electronegative methoxy groups of the MEH-PPV (MEH@CS NPs). Finally, the organic solvent was eliminated by evaporation, resulting in the formation of a stable colloidal nanoparticle dispersion. Dynamic light scattering (DLS) data showed an average size of 57 ± 12 nm (PDI 0.13) and 107 ± 6 nm (PDI 0.2) for MEH and MEH@CS NPs, respectively. The ZP of the MEH NPs was −38 ± 1 mV, whereas the MEH@CS NPs exhibited a ZP of +23 ± 4 mV, confirming the successful surface charge inversion and the effective coating with CS. Spherical nanoparticles with good monodisperse dimensions, similar to those found by DLS, were observed by scanning electron microscopy (SEM) and transmission electron microscopy (TEM) for both MEH (Fig. 1A-C) and MEH@CS NPs (Fig. 1D-F). Notably, TEM and STEM images revealed a lower electron density shell for MEH@CS NPs (Fig. 1E-F) compared to MEH NPs (Fig. 1B-C), which suggested the presence of CS coating around the NPs.

The absorption and emission spectra of colloidal MEH and MEH@CS NPs in water were compared to the spectra of the non-structured copolymer dissolved in THF. The absorption spectra of both NPs suspensions were slightly red-shifted (λ_{max}^{abs} = 499 nm) with respect to the spectrum of the MEH-PPV dissolved in THF (λ_{max}^{abs} = 488 nm) (Fig. 1G). This fact was mainly attributed to the conformational changes experienced by the polymer chain within the NPs originated by aggregation-induced intra- and intermolecular chain interactions [33,58]. This bathochromic shift was more evident in the emission profile (Fig. 1H) (λ_{exc} = 490 nm) as both NPs showed a significant red-shifted spectra (λ_{max}^{emi} = 595 nm) compared to that of the THF copolymer solution (λ_{max}^{emi} = 553 nm). This fact has been attributed to interchain energy transfer from high-energy to lower-energy domains, characterized by a higher degree of aggregation and larger electronic delocalization [58]. By

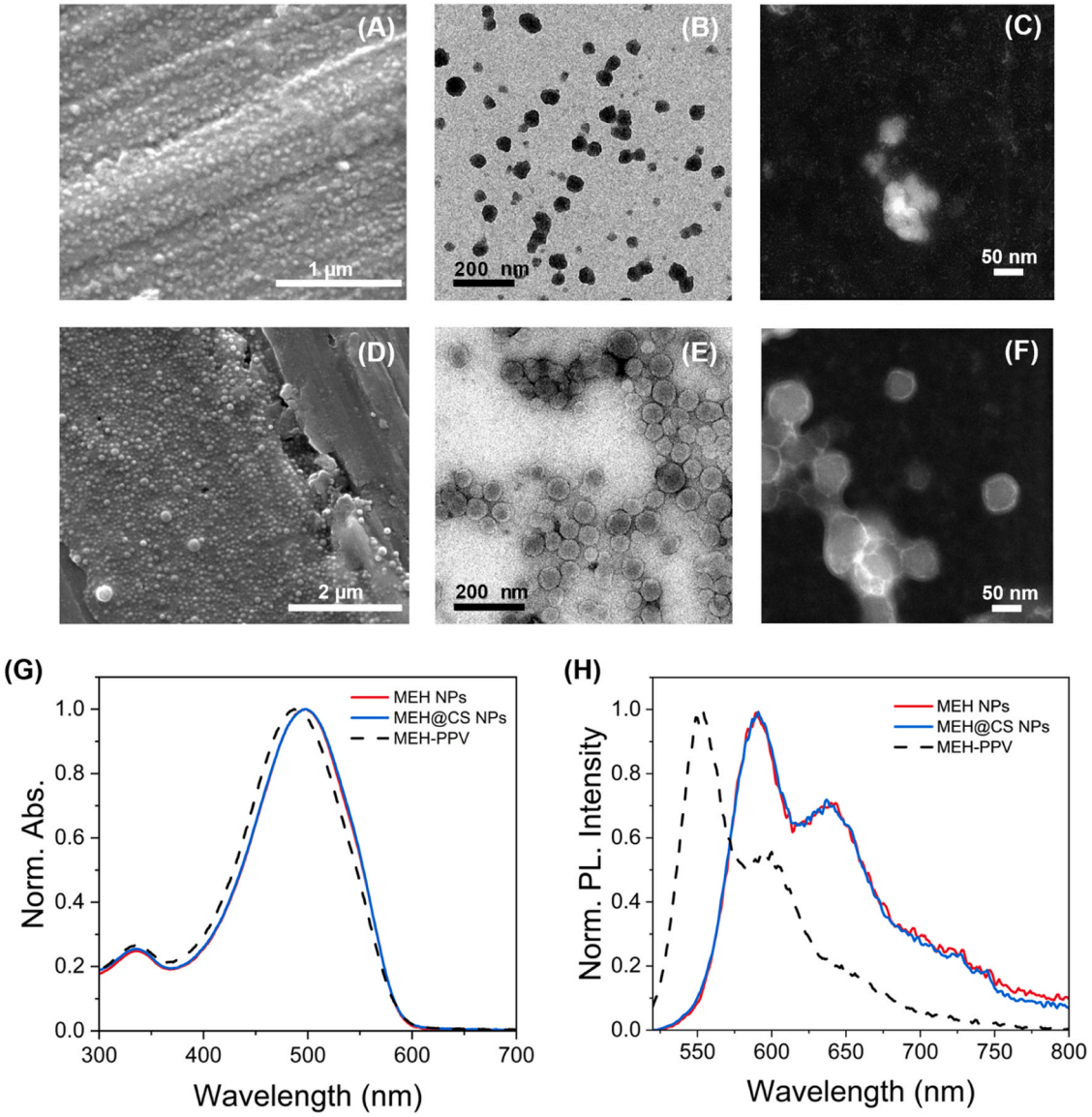

Fig. 1. MEH-PPV-based NPs. (A) SEM, scale bar = 1 µm, (B) TEM, scale bar = 200 nm, and (C) STEM, scale bar = 50 nm; images of MEH NPs. (D) SEM, scale bar = 2 µm, (E) TEM, scale bar = 200 nm, and (F) STEM, scale bar = 50 nm, images of MEH@CS NPs. (G) Absorption and (H) emission spectra of MEH-PPV copolymer in THF (λ_{max}^{abs} = 488 nm and λ_{max}^{emi} = 553 nm, black dashed lines), MEH and MEH@CS NPs water suspensions (λ_{max}^{abs} = 499 nm and λ_{max}^{emi} = 595 nm, red and blue lines, respectively). Both the MEH-PPV solution and the NP suspensions were excited at λ_{exc} = 490 nm.

changing the excitation wavelength (e.g., λ_{exc} = 365 nm), the recorded emissions slightly changed their intensities but not the spectra profiles, which means that the same emitting species is excited at the two wavelengths (Fig. S1). Comparable quantum yield (QY) values for MEH (8.6 %) and MEH@CS NPs (9.4 %) were obtained, but lower when compared to the bulk MEH-PPV solution (26 %). This reduction in QY can potentially be ascribed to reabsorption and quenching effects due to the aggregation of the polymer chains, common of conducting polymer NPs and films [33].

3.2. Chemical and colloidal stability

It is well known that MEH-PPV in solution undergoes chain scission through photo-oxidation processes activated by daylight [34,59,60]. Therefore, to assess their light fastness during the laboratory manipulation experiments, the colloidal dispersions of MEH NPs and MEH@CS NPs were exposed to ambient light at room temperature for an extended 15-day period. According to the DLS data, a decrease of ≈ 20 nm in size for MEH NPs, along with a noticeable Zeta Potential (ZP) decrease down to ≈ −11 mV for both NPs, was found (Figs. S2A-B). After 15 days, a ≈ 25 % and ≈ 40 % loss in absorbance for MEH and MEH@CS NPs, respectively, was detected (Figs. S2C-D), which may suggest that the NPs could be unstable during this period. The decrease was faster for the fluorescence (Figs. S2E-G), fact ascribed to the emission quenching caused by the formation of little amount of photodegradation products, yet enough to quench the fluorescence of the MEH PPV polymer. For both comparison purposes and to evaluate their shelf life over an extended period, the experiment was repeated with an aliquot of the same batch of redispersed NPs but this time in the absence of light (shielding the suspensions from light with Al foil) at 4°C. In this case, NPs did not experience any significant alteration in NPs size, ZP or spectral properties (as shown in Figs. S2A-G), confirming a stability even higher than that of MEH-PPV bulk solutions [34]. All in all, NPs are stable enough to be manipulated during the preparation experiments but preferably stored in water at 4 ºC in dark conditions to minimize the aging effect impact. The experiment in absence of light was repeated again with the same batch of NPs, but this time using a phosphate buffer saline (PBS) at pH 7.4 (isotonic buffer commonly used in cell culture to maintain pH and minimize osmotic shock in living cells) [61]. Under these conditions, NPs displayed a significant increment in size (> 800 nm), especially for MEH@CS NPs, tending to form larger aggregates visible to the naked eye. This was accompanied by a ZP decrease, which manifested a negative surface charge with average values of −28.6 ± 2.1 mV and −13.7 ± 5.8 mV for MEH and MEH@CS NPs, respectively (as shown in Figs. S2A-B). Furthermore, the intensity of both absorption and fluorescence significantly decreases due to the NP precipitation (Figs. S2H-K), most likely due to the salt-induced shielding effect of the repulsive electrostatic forces [61], and the consequent formation of larger aggregates.

According with these results, a meticulous colloidal stability assessment was also tested in cell culture media. For this reason, the experiments under dark conditions were repeated at 37 ºC for 3 days, incorporating now 10 % fetal bovine serum (FBS) and incubated in different simulated biological environments: i) in PBS [62] at pH 7.4, which mimics extracellular conditions[61], ii) at pH 5.7, simulating intracellular conditions [61], and iii) in MEM-α cell culture medium without red phenol (pH 7.0). Water suspensions of both NPs at 37 ºC were also measured as a control reference. In all the cases, both MEH and MEH@CS NPs consistently maintained ZP values around ≈ −11 mV, in contrast to the control water suspensions (-43.7 ± 1.2 mV and 29.6 ± 1.3 mV for MEH and MEH@CS NPs, respectively). These results support the formation of an outer negatively charged FBS protein corona around the NPs, hindering their intrinsic surface charge (Figs. S3A-B) [47,61,63,64]. More differences were found for their NP size. MEH@CS NPs redispersed in PBS show notable variations attributed to the pH-induced conformational changes in the CS shell (Fig. S3C, day 0). At acidic pH, a volume expansion (and therefore a thicker protein corona) is found as a result of the repulsions between the protonated amino groups of the CS coating (CS isoelectric point = 6.3 [47]). On the contrary, at alkaline pH, the CS structure shrinks due to the reduction in the repulsive forces between those groups, causing less attraction of the negative serum proteins on the NPs' surface. The size of MEH NPs was not affected by the pH, as expected (Fig. S3D). After a 3-day incubation period at 37 ºC, NP aggregation was observed upon incubation with PBS (see Figs. S3C-D), induced by the shielding effect of the salt, as was previously mentioned, affecting their colloidal stability (see Figs. S2A-B) and optical properties (see Figs. S2H-K). No aggregates were formed for both MEH and MEH@CS NPs in water or MEM-α cell culture media, and no significant variations in absorbance and fluorescence intensity throughout 3 days were observed in MEM-α at 37 ºC (Figs. S3E-F), confirming their colloidal stability.

3.3. Cellular uptake and intrinsic cytotoxicity

The intrinsic cytotoxicity of MEH and MEH@CS NPs was assessed in two distinct inflammatory cell line models: i) the mouse macrophage RAW264.7 cells, traditionally used to study anti-inflammatory drug activity as they produce abundant cytoplasmic HOCl [16,18,54], and ii) the well-known human cervical carcinoma HeLa cells, recognized for their elevated production of HOCl compared to that in normal cells, which in fact acts as a pivotal signaling regulator for proliferation across numerous cancer cell lines [15,17]. The NPs exhibit concentration-dependent cytotoxicity in the RAW264.7 cell line after both 24 and 48 h of incubation, displaying a half-maximal toxicity concentration (IC50) of 68 ± 3 and 56 ± 1 μg mL^{-1}, for MEH and MEH@CS NPs, respectively (Fig. 2A). In HeLa cells, notably, we observed minimal cytotoxicity within the tested range. This resulted in significantly lower toxicities, showcasing a survival rate of over 75 % under similar experimental conditions (Fig. 2B). These results emphasize the good biocompatibility of the NPs at concentrations below ≈ 50 μg mL^{-1} reinforcing their suitability for cellular applications.

Cellular uptake of MEH@CS and MEH NPs (30 μg mL^{-1}) in RAW264.7 and HeLa cell lines after 24 h of incubation was analyzed by epi-fluorescence and confocal microscopies and flow cytometry assays, which provide quantitative validation of the uptake. In all the cases, intracellular fluorescence emission (λ_{exc} = 470 nm, green channel for epi-fluorescence microscopy) was observed, though it was especially remarkable for MEH@CS NPs (Fig. S4). Indeed, the intensity of the fluorescent signal detected for MEH@CS NPs in both cell lines, which directly correlates to the number of internalized NPs[65], was found to be approximately two orders of magnitude higher for the coated nanoparticles (Fig. 2C-D). These results were supported by confocal microscopy assays. XZ-YZ stack images confirmed the intracellular localization only for MEH@CS NPs on both cell lines and discarded any fluorescence emission coming from the cell surface (Fig. 2E). Such a difference in cell internalization for both families of NPs has been tentatively attributed to the differential surface charge of the NPs. Positively charged MEH@CS NPs exhibited faster uptake via electrostatic attractions, especially in conditions of passive targeting [66–70]. These results agree with the lower toxicity within the cell lines (p = 0.023) of MEH NPs (see Fig. 2A-B).

Given that HOCl primarily originates in the mitochondria [71], further MEH@CS NPs co-localization experiments were conducted using epi-fluorescence microscopy together and a mitochondrial tracker (see Methods section). Internalized MEH@CS NPs fluorescence emission (green channel, λ_{exc} = 470 nm) displayed a notable overlap with the mitochondrial dye fluorescence (red channel, λ_{exc} = 525 nm, as evidenced in the merged image Fig. 3A, for both cell lines. Moreover, a robust Pearson's correlation coefficients (PCC) of 0.91 and 0.96 were obtained for RAW264.7 and HeLa cells, respectively (see Fig. 3A). Furthermore, colocalization experiments using a confocal microscope were carried out and the results suggest that NPs potentially reach the

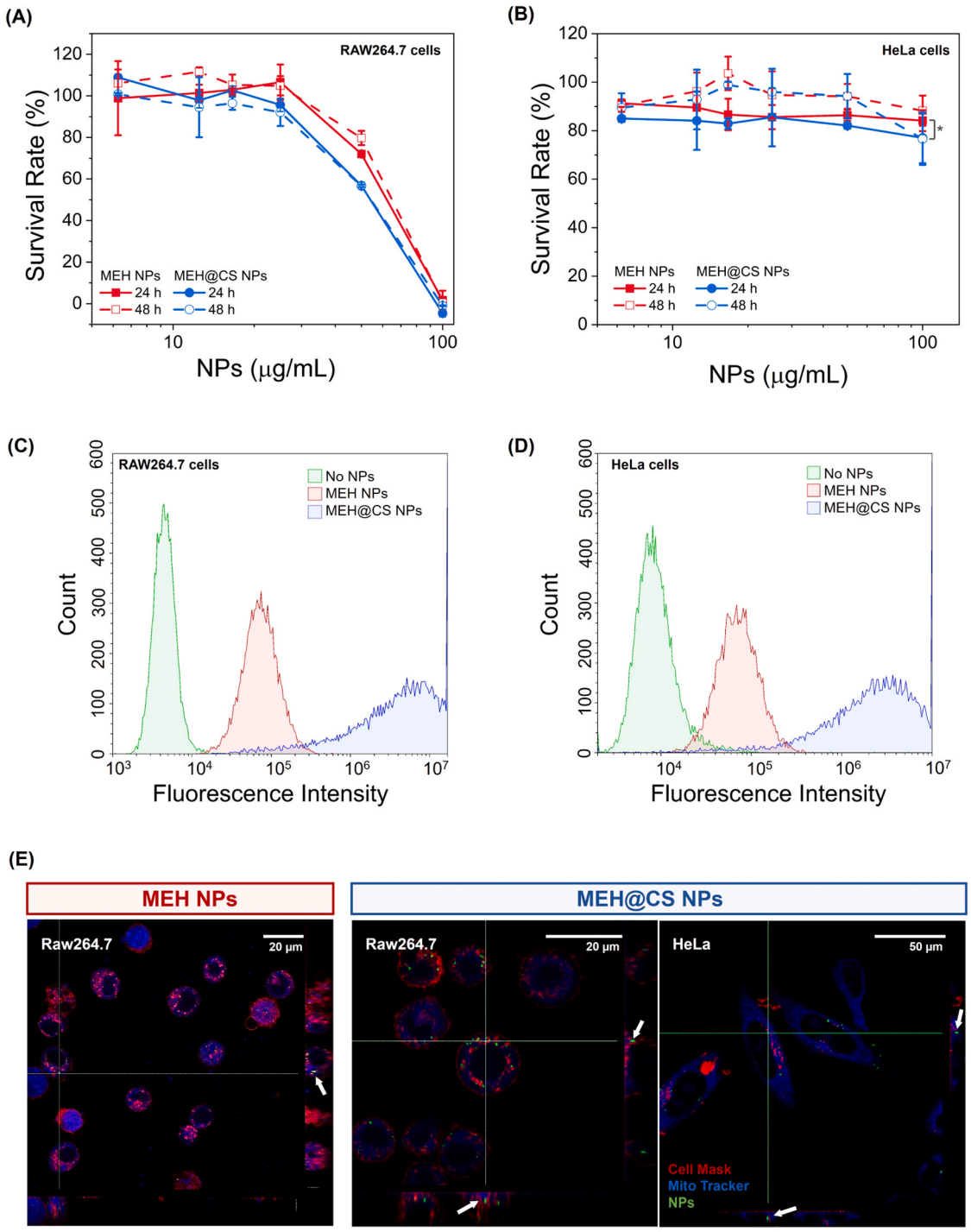

Fig. 2. *In vitro* biological characterization of MEH-PPV-based NPs. Survival Rate of (A) RAW264.7 macrophages and (B) HeLa cells, exposed to different concentrations of MEH@CS (blue dots) and MEH NPs (red squares) for 24 (solid symbol) and 48 h (empty symbol) ($n = 3$). Statistical analysis via a two-tail Student's t-test. *$p < 0.05$; otherwise no statistically significant difference. Fluorescence intensity histogram analysis of (C) RAW264.7 macrophages and (D) HeLa cells, incubated for 24 h with 30 μg mL^{-1} of MEH NPs (red) and MEH@CS NPs (blue). Cells without NPs (green) were used as control. (E) Confocal microscope average projection of a stack of images of RAW264.7 cells after 24 h incubation with MEH NPs and MEH@CS NPs (30 μg mL^{-1}); respectively, and HeLa cells after 24 h incubation with MEH@CS NPs (30 μg mL^{-1}) (green = NPs, red = plasma membrane, blue = mitochondria). White arrows pinpointing the location for the YZ (vertical) and XZ (horizontal) axes projections, confirming NPs presence within the cytoplasm. Scale bars, 20 μm for RAW264.7 and 50 μm for HeLa.

mitochondria (Fig. 3B). These results are in agreement with previous studies showing preferential mitochondrial localization for small (1–100 nm) CS-coated NPs on several cell lines, including RAW264.7 macrophages [69–77],

3.4. HOCl sensitivity and selectivity in bulk suspensions

HOCl detection by MEH and MEH@CS NPs colloidal dispersions (23 μg mL^{-1}) was monitored following its absorption and fluorescence progression over time at three fixed acid concentrations (10, 100, and 1000 μM). Noticeably, both NPs exhibited a rapid absorption intensity

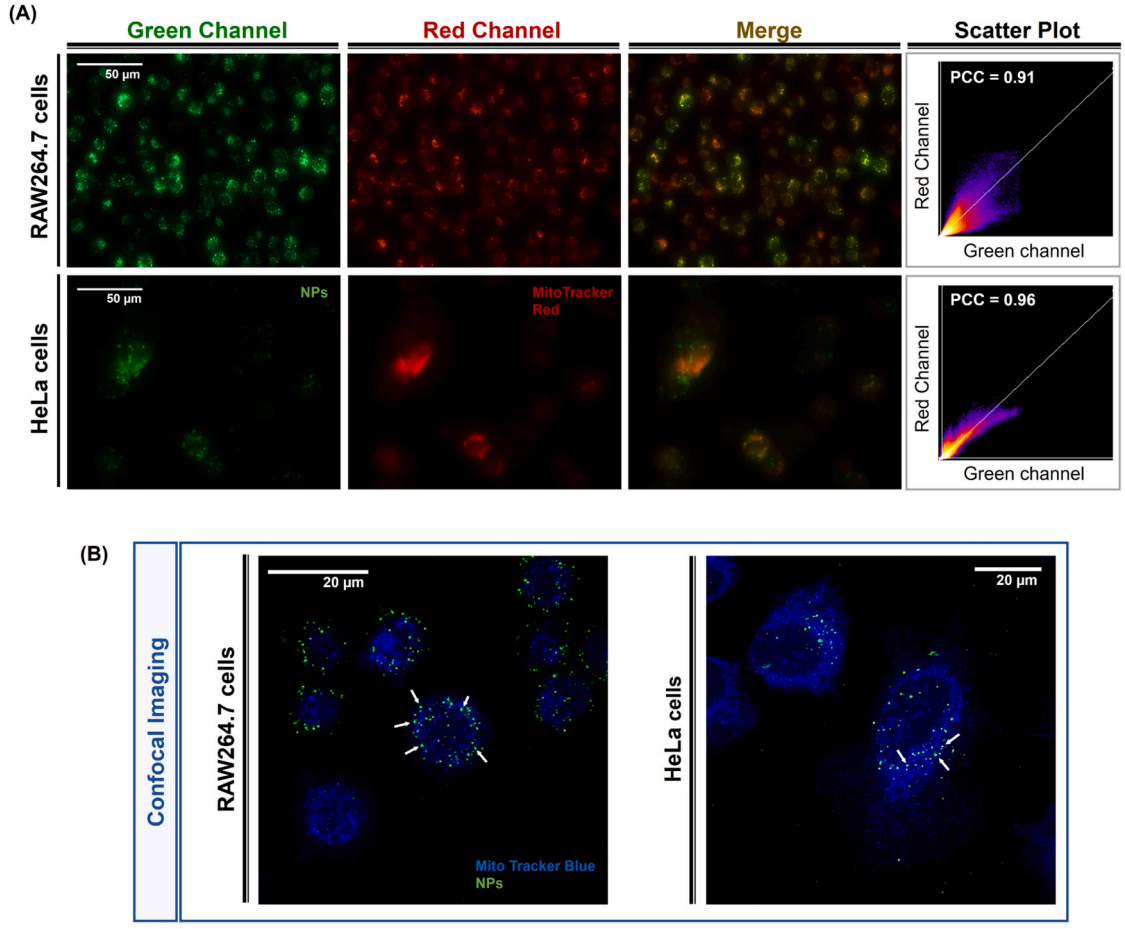

Fig. 3. Colocalization of MEH-PPV-based NPs in living cells. RAW264.7 macrophages and HeLa cells were incubated for 24 h with MEH@CS NPs (30 µg mL^{-1}) and washed before imaging for mitochondrial staining. (A) Live cell imaging performed by fluorescence microscopy. Green channel (534/56 nm band pass emission, 470/40 nm band pass excitation): MEH@CS NPs, red channel (587/58 nm band pass emission, 525/50 nm band pass excitation): MitoTracker red for mitochondria. Merged image of green and red channels displays the colocalization of NP-mitochondria (in yellow). Scatter plot shows the correlation diagram between green and red channels. Scale bars = 50 µm. (B) Live cell confocal images (green = NPs, blue = BioTracker blue for mitochondria). White arrows point to the possible colocation of NPs-mitochondria. Scale bars = 20 µm.

decrease that stabilizes after 30 min, regardless of the HOCl concentration (Figs. S5A-B). However, the precise estimation of its fluorescence time response at HOCl concentrations of 100 and 1000 µM was prevented due to the rapid fluorescence sensitivity to this acid and subsequent rapid emission quenching (Figs. S5C-D). Finally, the fluorescence kinetics was evaluated for the lowest HOCl concentration of

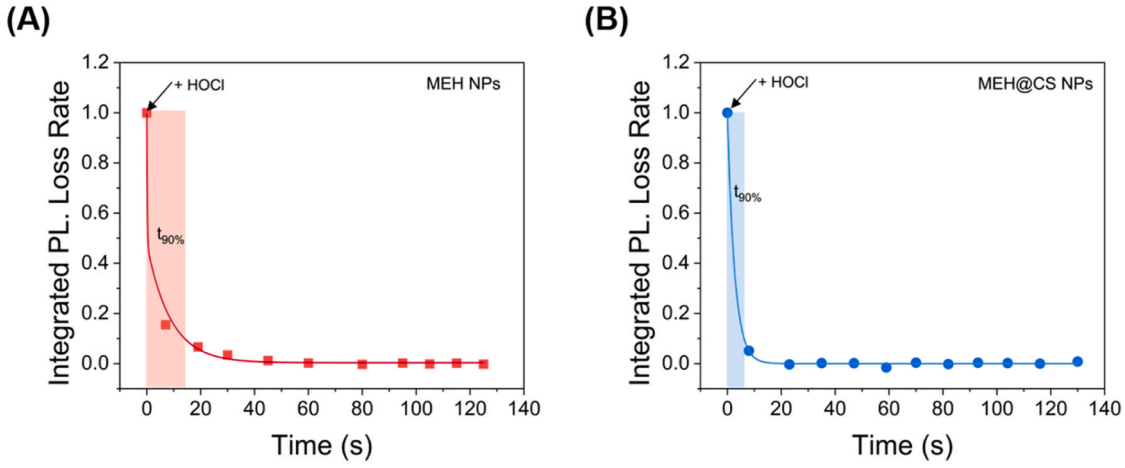

Fig. 4. Time-dependent responses of the fluorescence intensity of MEH-PPV-based NPs exposed to HOCl. Time evolution of the integrated fluorescence intensity loss rate (λexc= 490 nm) of MEH (A) and MEH@CS NPs (B) (23 µg mL^{-1}) upon addition of a low concentration of HOCl (10 µM). The data were calculated using the formula: Integrated PL. Loss Rate = $[I(t) - I_{steady})/ (I_0 - I_{steady})]$. Data points were fitted on origin using nonlinear curve fit.

10 μM. The integrated fluorescence intensity decreases quickly reaching a minimum value and an equilibrium state within 40 s and 20 s for MEH and MEH@CS NPs, respectively (Fig. 4 and S6). The $t_{90\ \%}$, determined as the time required for the NPs to reach 10 % of the intensity difference between the emission at t_0 (I_0, before exposure to HOCl) and the fluorescence at the steady state (I_{steady}), does not change with time. For both NPs this value was determined to be less than 20 s (Fig. 4), thus, as far as we know it is comparable or even faster than other reported HOCl probes[7], and confirm that both NPs could be utilized for nearly real-time detection of HOCl

The experiments were repeated at pH 5.7 (intracellular pH) and a fixed HOCl exposure time of one hour (well above the stabilization time for both absorption and fluorescence optical properties), while increasing the acid concentration up to ≈ 200 μM (Fig. 5A-B and S7A-C). UV–vis spectra of both NPs showed a linear decrease in absorption (Figs. S7D-E) and a noteworthy blue shift of the maximum from λ_{max}^{abs} = 490 nm to 360 nm, which overall yielded discoloration of the NP suspensions (see Fig. 5A and S7A-B). The linear absorbance decrease can be directly related to the concentration reduction of the MEH-PPV within the NPs, due to its HOCl-induced degradation. Concomitantly, fluorescence intensity underwent a significant and faster reduction (λ_{max}^{emi} = 595 nm), even at the lowest tested HOCl concentration (see Fig. 5B and S7C). The fast emission loss was ascribed to the MEH-PPV concentration decrease and its emission quenching (via photoinduced electron transfer processes), caused by species formed from the degradation that act as electron trapping centers [78]. Energy transfer from the MEH-PPV to the formed species was instead discarded as the degraded NPs absorb at shorter wavelengths (higher energies), resulting energetically impossible any Förster Resonance Energy Transfer or radiative reabsorption. Triplet-triplet energy transfer was also discarded since the measurements were carried out under air atmosphere, thus under conditions of very short lifetime of triplet states. All in all, both absorption and emission spectra exhibit significant changes, though fluorescence was the preferred technique as its fast and sudden changes allow for a quicker determination of weaker HOCl variations.

Next step aimed to estimate the detection limit (LOD), minimum HOCl concentration that can be reliably detected, for both MEH and MEH@CS NPs. The detection dynamic range is comprised between the lowest concentration measurable distinguishable from zero, defined as the lower limit of detection (LOD_{min}), and the largest detectable one within a linear response range (LOD_{max}) [79,80]. Therefore, to estimate the detection dynamic range, fluorescence emission spectra of aqueous suspensions of NPs (23 μg mL^{-1}) at pH 5.7 (intracellular pH) were recorded after 1 h of exposition to several HOCl concentrations. A concentration range with a linear response was identified by applying a natural log-log transformation approach to the data (Fig. 5C and S7F). The integrated emission of both families of NPs displayed a good linear correlation with the HOCl concentration on the natural log-log scale

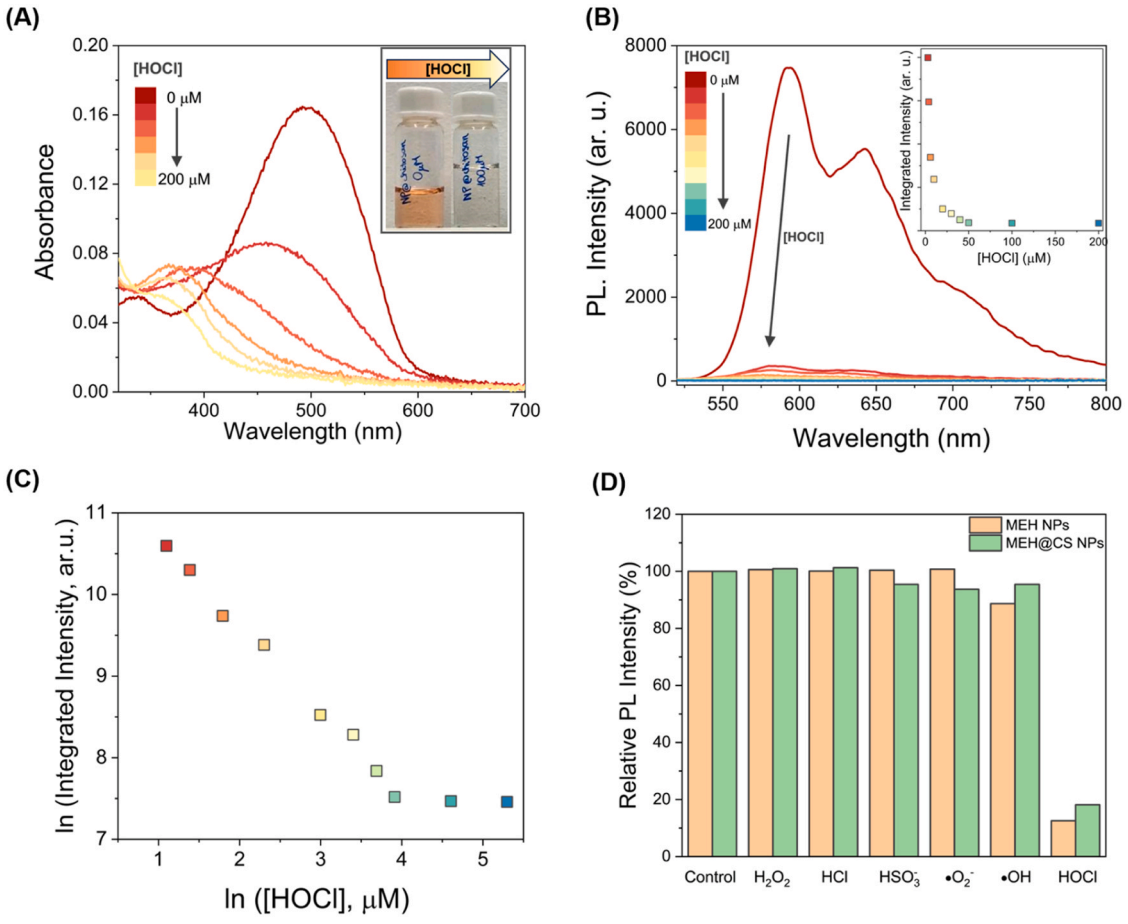

Fig. 5. Absorption and fluorescence responses of MEH-PPV-based NPs towards HOCl. (A) UV–vis absorption spectra of MEH@CS NPs (23 μg mL^{-1}) at pH 5.7 exposed for 1 h to different concentrations of HOCl (0 – 200 μM), inset: color change of the MEH@CS NPs suspension after HOCl exposition (100 μM). (B) Fluorescence spectra of MEH@CS NPs (23 μg mL^{-1}) (λ_{exc} = 490 nm) at pH 5.7 after exposition for 1 h to solutions of different HOCl concentrations (0 – 200 μM), inset: decay plot of the corresponding integrated fluorescence intensities of the MEH@CS NPs suspension exposed to different concentrations of HOCl. (C) Log-Log plot, on a natural log scale, of the integrated emission intensity of MEH@CS NPs against the HOCl concentration (μM) of the different solutions used. (D) Relative fluorescence intensity ($\lambda_{exc/em}$ = 490/595 nm) of MEH (orange) and MEH@CS (green) NPs (23 μg mL^{-1}) towards H_2O_2 (100 μM), HCl (15 μM), HOCl (15 μM), HSO_3^-(15 μM), $•O_2^-$ (15 μM), and •OH (15 μM) in phosphate buffer (pH 5.7).

below ≈ 60 μM and ≈ 90 μM (concentrations after which the change in fluorescence intensity becomes negligible, reaching a plateau at the bottom of the curve), for MEH@CS ($R^2 = 0.994$) and MEH ($R^2 = 0.96$) NPs suspensions, respectively (Fig. 5C and S7F). From here, LOD_{min} values were determined using the equation $3\sigma/k$, where k is the slope in the observed linear range on the natural log-log curve, and σ is the fitting error on the intercept [17,18,25,27]. LOD_{max} values were determined by the cross-point between the natural log-log linear curve and the noise background plateau curve [81]. Thus, the resulted dynamic intervals (LOD_{min}, LOD_{max}) for MEH and MEH@CS NPs were calculated to be (0.784, 83 ± 4) μM and (0.384, 55 ± 3) μM, respectively, similar to others found in ON-OFF fluorescence molecular probes[7], both indicating detection capabilities over the normal physiological concentration range of 5 – 25 μM [18,81].

Finally, and for comparison purposes, the reactivity of both MEH NP and MEH@CS NPs towards other common reactive species present in biological systems (H_2O_2, HCl, HSO^{3-}, hydroxyl radical (•OH), and superoxide anion ($\bullet O_2^-$)) was studied as done for HOCl (Fig. 5D and S8), These species could competitively oxidize and degrade the MEH-PPV polymer, contributing to their optical property variations and interfering with the correct estimation of HOCl concentration [5–7]. As depicted in Fig. 5D, no significant fluorescence variations were detected for any of the tested species, corroborating the good selectivity of the MEH-PPV-based NPs towards the HOCl.

3.5. Detection of endogenous HOCl reactivity in living cells

The intracellular HOCl detection abilities of MEH and MEH@CS NPs (30 μg mL^{-1}) were examined in both HeLa cells and RAW264.7 macrophages by monitoring fluorescence changes using flow cytometry. To stimulate the generation of intracellular HOCl, lipopolysaccharide (LPS) from *Escherichia coli,* supplemented with phorbol 12-myristate 13-acetate (PMA) were used[14–17,25–27]. LPS is an endotoxin that triggers inflammation, leading to the production of ClO^- via myeloperoxidase (MPO) pathway[14,19]. PMA stimulated the Nicotinamide adenine dinucleotide phosphate (NADPH)-oxidase route, resulting in the production of H_2O_2[1,82]. Non-stimulated cells and cells stimulated without NPs were used as blanks. Control groups treated with only LPS/PMA (without NPs), did not show any significant emission changes.

Following stimulation with a fixed PMA amount (1 μg mL^{-1}), internalized MEH@CS NPs in HeLa cells exhibited a significant fluorescence decrease as LPS concentration increases (0–10 μg mL^{-1}) reaching a plateau from where the emission became independent of the LPS concentration (Fig. S9A). This implies that for this kind of tumoral cell, endogenous H_2O_2 acts as a limiting factor for HOCl production, despite MPO representing the main route for its generation under the evaluated conditions. Thus, to increase the peroxide precursor concentration and catalyze more HOCl, PMA concentration was varied (0–2 μg mL^{-1}), while LPS concentration was kept constant (1 μg mL^{-1}). At these conditions, a decrease in fluorescence intensity for MEH@CS NPs was observed with increasing PMA concentration, displaying a correlation with the emission variation detected (Fig. S9B). Unexpectedly, elevated concentrations of PMA (≥ 10 μg mL^{-1}) showed a slight increase in the NPs emission. This phenomenon could be attributed to the reported toxicity of high intracellular H_2O_2 and HOCl levels, induced by the excess PMA used, which, in turn, triggers cell apoptosis and detachment [83]. Consequently, the detected emission arises predominantly from non-discarded cells after the wash procedure, minimally influenced by PMA. The observation of apoptotic bodies under optical microscopy further supports this hypothesis at these PMA concentrations.

Notably, for MEH@CS NPs incubated on RAW264.7 cells, an apparent linear emission decrease was observed upon an increase in LPS concentration (0–10 μg mL^{-1}), at a fixed PMA amount (1 μg mL^{-1}) (Fig. 6A), suggesting a correlation between intracellular HOCl production and the emission variation from MEH@CS NPs, particularly when LPS concentrations remained below 10 μg mL^{-1}. Similar to the observation at high PMA concentrations in HeLa cells, an increase in NPs emission was detected at the highest LPS level (10 μg mL^{-1}). This increase is attributed to the substantial rise in intracellular HOCl concentration resulting from elevated LPS levels, which leads to cell apoptosis and detachment[19,29,84]. This outcome was corroborated by both optical microscopy and flow cytometry, displaying emissions solely from the cells that were not discarded during the wash procedure and thus less affected by the endotoxin treatment.

On the other hand, when MEH NPs were internalized in both cell lines, they showcased insignificant fluctuations in fluorescence emission on HeLa cells upon variation of PMA ($p > 0.4$ vs. control) or LPS concentration ($p > 0.2$ vs. control), as well as on RAW264.7 macrophages (p

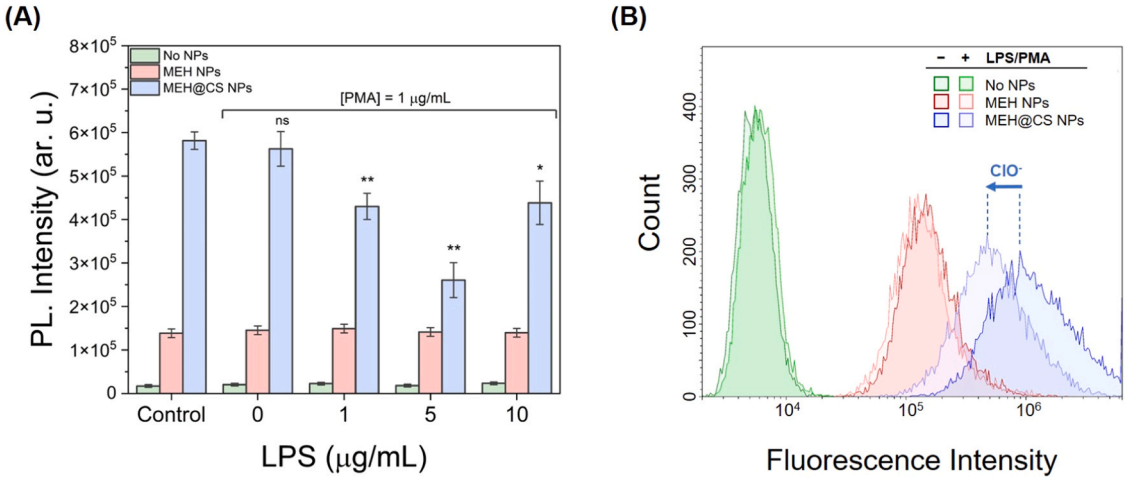

Fig. 6. Endogenous HOCl detection by MEH-PPV-based NPs. (A) Median fluorescence intensity values from RAW264.7 macrophages incubated for 24 h with MEH (red bars) and MEH@CS NPs (blue bars) (30 μg mL^{-1}). Endogenous HOCl was generated upon the addition of LPS solutions of different concentrations (0–10 μg mL^{-1}) and, after 6 h, PMA solutions (1 μg mL^{-1}). RAW264.7 macrophages without NPs (green bars) were used as a control. Cells without LPS/PMA treatment were used as negative controls. Statistical analysis vs. control via two-tail Student's t-test: *$p < 0.05$; **$p < 0.01$; *ns* means no statistically significant difference. (B) Fluorescence intensity histogram analysis of RAW264.7 macrophages incubated without NPs (green), MEH (red) and MEH@CS (blue) NPs (30 μg mL^{-1}) for 24 h. Endogenous HOCl was generated by stimulation with LPS (5 μg mL^{-1}) and PMA (1 μg mL^{-1}) (lighter colors). Cells without stimulation (darker colors) were used as negative controls. Fluorescence values in all experiments were determined by flow cytometry ($n = 3$) and acquired with a PE filter (585/42 nm band pass).

> 0.3 vs. control). This was plausibly attributed to the limited uptake of the NPs and their higher upper limit of detection (LOD_{max}) (≈ 83 μM), both contributing to a low NP emission signal in the cells that avoids any possible determination of intensity changes (see Fig. 6 and S9). Considering this, HeLa cells are known to express notably diminished MPO levels, and was reported that they produce approximately 19 times less HOCl than RAW264.7 macrophages during a bacterial infection [16]. Thus, these findings effectively underscore the potential of MEH@CS NPs in detecting endogenous HOCl, even within cellular contexts marked by reduced MPO levels, as observed in HeLa cells.

3.6. Encapsulation of the HOCl scavenger quercetin (QCT)

As shown above, exposure of the NPs to HOCl induces the degradation of the MEH-PPV polymer, provoking simultaneous NP disintegration. This HOCl-triggered effect could thus be used not only to detect but also to self-release pre-encapsulated drugs, allowing for the auto-equilibration of the overproduced intracellular HOCl levels. Therefore, next, the aim was to obtain NPs of MEH-PPV encapsulating the water-insoluble HOCl scavenger quercetin (QCT). Attempts to obtain QCT-containing MEH and MEH@CS NPs (QCT-MEH and QCT-MEH@CS NPs) were done by dissolving the desired amount of the drug in the organic phase together with the MEH-PPV copolymer, prior to the emulsification step, and following the protocol previously described (see Methods for more details). The syntheses were optimized using different MEH-PPV:QCT molar ratios ranging from 1:18–1:36. In the case of QCT-MEH NPs, TEM and SEM images of the different molar ratios explored unveiled the formation of a non-structured material plus needle-shaped crystals (0.5 – 5 μm), lacking nanoparticles in all the cases (Fig. S10A). The needle-like structures were attributed to the segregation and crystallization of the excess of QCT present in the organic phase, during the emulsification [85–88]. This was further corroborated by provoking direct crystallization of QCT from THF solutions (the same solvent used for the NPs synthesis), which gave similar needle-like structures.

Attempts to synthesize QCT-MEH@CS NPs with MEH-PPV:QCT molar ratios exceeding 1:27 also evidenced morphological deformations of the NPs as well as the appearance of needle-like crystals. More promising were the results obtained from the syntheses with MEH-PPV:QCT molar ratios below 1:27 (Fig. S10B), where the intricate charge balance between the three components was likely maintained [89]. TEM and SEM images showed the presence of spherical nanoparticles with dimensions of 108 ± 9 nm, very similar to those found for native MEH@CS NPs (see Fig. 1D-F). These results suggest that above a certain concentration, the QCT destabilizes the nanoemulsion, diffusing out to the water and forming crystals. In contrast, at lower concentrations, it remains dissolved in the solvent during the MEH-PPV precipitation, trapping the drug. To confirm the QCT encapsulation, optical characterization of the NPs was done. Compared to the QCT-free NPs, the absorption spectrum of the QCT-containing NPs manifested an increment of absorbance at 372 nm attributed to the QCT absorption (Fig. S10C)[42,46]. This variation was used to quantify the amount of QCT encapsulated (see Materials and Methods section). The drug loading rate (DL) and encapsulation efficiency rate (EE) of the QCT-MEH@CS NPs obtained using MEH-PPV:QCT molar ratios below 1:27 were quantified (see Table 1 and SI for further details), reaching maximum values of 3.91 % and 27.1 %, respectively. It is also worth mentioning that, the encapsulation of QCT in MEH@CS NPs induces a fivefold increase in their water solubility, from 2.15 μg mL^{-1} at RT (intrinsic solubility in water [90]) to 11 μg mL^{-1} in its encapsulated form (QCT-MEH@CS NPs). Finally, no significant changes were observed in the emission spectra of QCT-MEH@CS NPs (Figs. S10D), indicating that QCT is not affecting the nanostructuration and stacking of MEH-PPV polymer chains, neither induce undesired emission quenching phenomena of the polymer.

Table 1
Averaged QCT mass measured, drug loading (DL) and encapsulation efficiency (EE) for the QCT-MEH@CS obtained using different MEH-PPV:QCT molar ratios (n = 5).

Molar ratio	QCT mass (μg)	DL (%)	EE (%)
1:18	6.0 ± 1.5	1.18	11.9
1:24	11.1 ± 4.7	2.18	17.1
1:25	13.1 ± 3.3	2.56	18.8
1:27	20 ± 14	3.91	27.1

A preliminary assay of stimuli-triggered release of encapsulated QCT was conducted by exposing a bulk suspension of QCT-MEH@CS (75 μg mL^{-1} with a MEH-PPV:QCT molar ratio of 1:27) to 1 mL of HOCl (600 μM) for 1 h (after this time the NPs suspension turned colorless). Noteworthy SEM images of the treated NPs showed no spherical NPs but cubic crystals (50–700 μm) attributed to free QCT (Fig. S11A). The change in morphology for the QCT crystals with respect to the previously obtained needle-like structures is not unexpected. It is already reported that QCT adopts different crystalline structures (needles-like and cubic), depending on the crystallization conditions, kinetics and whether it incorporates water molecules into its lattice during crystal growth[91,92]. In any case, to corroborate these results, further experiments were done by exposing QCT-free NPs to HOCl. In this case, beyond the amorphous material resulting upon decomposition of the MEH-PPV polymer, no additional cubic or needle-like crystalline material was found (Fig. S11B).

3.7. In vitro HOCl inhibition by QCT-MEH@CS NPs

To investigate the potential anti-inflammatory effect of QCT-MEH@CS NPs, RAW264.7 macrophages were selected as suitable *in vitro* model due to their ability to produce *high* levels of *HOCl* after stimulation with *LPS/PMA*[29,43]. More specifically, the dose-dependent effect of the drug released from the QCT-MEH@CS NPs was studied in order to evaluate its cytotoxicity.

For this, RAW264.7 macrophages were incubated with the NPs (30 μg mL^{-1}) obtained from several MEH-PPV:QCT molar ratios (1:18 – 1:27) during 24 and 48 h (Fig. 7A). A significant increment in the cellular survival rate (> 90 %) was observed compared with the MEH@CS NPs control (≈ 73 %) ($p < 0.05$). Furthermore, a notable increase in cell proliferation was noted at 48 h ($p = 0.03$), aligning with findings from previous studies with macrophages[93]. Worth mentioning, QCT-MEH@CS NPs also exhibited a substantially higher cell survival rate compared to free QCT (2 μg mL^{-1}) ($p < 0.03$) [45,93,94]. All in all, the successful intracellular delivery of the drug via passive diffusion was confirmed.

To test the *in vitro* inhibition of HOCl, macrophages were incubated with QCT-MEH@CS NPs (30 μg mL^{-1}) obtained at different MEH-PPV:QCT ratios under LPS (5 μg mL^{-1}) and PMA (1 μg mL^{-1}) stimulation. LPS/PMA-stimulated and non-stimulated cells were also exposed to MEH@CS NPs (QCT-free) as controls. Changes in NPs fluorescence emission from cells were evaluated by flow cytometry (Fig. 7B-C). As expected, all LPS/PMA-stimulated cells showed a decrease in fluorescence compared to non-stimulated cells containing MEH@CS NPs (control), due to the production of HOCl. The fluorescence intensity showed by LPS/PMA-stimulated cells incubated with QCT-MEH@CS NPs was higher than that of the LPS/PMA-stimulated cells incubated with QCT-free MEH@CS NPs, and increased with the amount of the loaded QCT ($p < 0.4$) (Fig. 7C). The higher fluorescence intensity was attributed to the rapid scavenging of HOCl by the QCT released from the MEH@CS NPs[43,95], which displays a lower degradation degree as a consequence of the reduction of the acid concentration (Fig. 7B). Furthermore, the increase in fluorescence emission from QCT-MEH@CS NPs with increasing QCT load gave a direct correlation of the optical signal with the QCT dosage (Fig. 7C), directly aligned with the HOCl downregulation[43,94].

Finally, to verify the anti-inflammatory role of QCT-MEH@CS NPs,

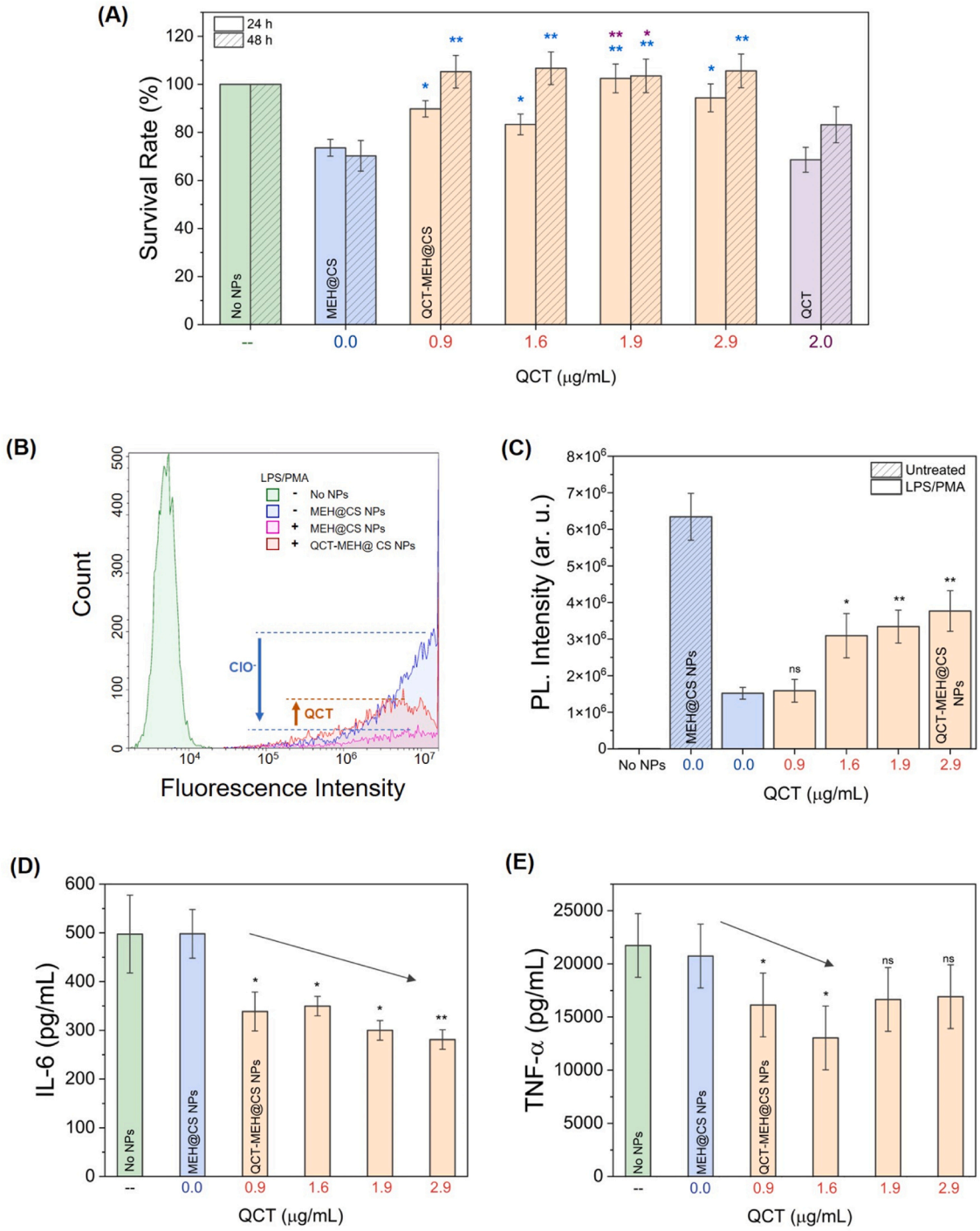

Fig. 7. Characterization of endogenous HOCl inhibition. (A) Cell Survival Rate of RAW264.7 cells exposed to QCT-MEH@CS NPs (orange) with different QCT loadings for 24 h (solid bars) and 48 h (hatched bars). Cells without NPs (green), cells exposed to free QCT (2 μg mL^{-1}) (violet), and cells incubated with MEH@CS NPs (blue) were used as controls. Statistical analysis for QCT-MEH@CS NPs vs. MEH@CS control (blue asterisk) and for NPs loading only 1.9 μg mL^{-1} of QCT vs. free QCT (violet asterisk). (B) Fluorescence intensity histogram analysis of LPS/PMA-stimulated RAW264.7 cells exposed for 24 h to MEH@CS (pink) and QCT-MEH@CS NPs at 1:27 molar ratio (red). Non-stimulated cells incubated with MEH@CS NPs (blue) and cells without NPs were used as controls (green). Fluorescence was acquired by flow cytometry with a PE filter (585/42 nm band pass). (C) Median fluorescence intensity values from RAW264.7 cells incubated with MEH@CS NPs (blue) without stimulation (hatched bar) and under LPS/PMA treatment (solid bar), and QCT-MEH@CS NPs (orange) with different QCT loadings under LPS/PMA stimulation. Cells without NPs were used as control (green). Fluorescence values were determined by flow cytometry with a PE filter. Levels of (D) IL-6 and (E) TNF-α cytokines produced by LPS/PMA-stimulated RAW264.7 macrophages incubated with MEH@CS (blue), and QCT-MEH@CS NPs with different QCT loadings (orange), measured by bead-based ELISA kit. Cells without NPs (green) were used as controls. All NPs concentrations were set at 30 μg mL^{-1}. Concentrations of 0.9, 1.6, 1.9 and 2.9 μg mL^{-1} of encapsulated QCT corresponded to the synthesis of NPs using MEH-PPV:QCT 1:18, 1:24, 1:25 and 1:27 molar ratios, respectively. LPS/PMA stimulation consisted of cell stimulation with LPS (5 μg mL^{-1}) and the addition of PMA (1 μg m^{-1}) after 6 h of LPS treatment. All the data were demonstrated as mean ± SD ($n = 3$). Statistical analysis vs. corresponding control via two-tail Student's t-test: *$p < 0.05$; **$p < 0.01$; *ns* means no statistically significant difference.

the quantification of the main pivotal pro-inflammatory cytokines, namely interleukin-6 (IL-6) and tumor necrosis factor-alpha (TNF-α), was carried out. These cytokines are closely linked to cellular oxidative stress caused by HOCl overproduction [43,95]. Levels of both cytokines were measured by flow cytometry in LPS/PMA-stimulated RAW264.7 macrophages through a bead-based ELISA kit (Fig. 7D-E). Cells exposed to MEH@CS NPs were used as NP control. LPS/PMA (at concentrations of 5 and 1 μg mL^{-1}, respectively) significantly increased IL-6 and TNF-α levels compared to both blank control groups (< 40 pg mL^{-1}), resulting in increments of 498 and 21732 pg mL^{-1}, respectively. Nevertheless, the elevated expressions of both pro-inflammatory cytokines underwent substantial reduction through treatment with QCT-MEH@CS NPs in a dose-dependent trend, reaching minimal values of 280 pg mL^{-1} (≈ 44 %) for IL-6 ($p < 0.04$), and 13036 pg mL^{-1} (≈ 40 %) for TNF-α ($p < 0.02$), in good agreement with other existing studies [43,95]. In summary, these results suggest that QCT-MEH@CS exhibits the capacity to reduce the levels of inflammatory mediators IL-6 and TNF-α within LPS/PMA-stimulated RAW264.7 macrophages, effectively inhibiting the inflammatory response.

4. Conclusion

MEH@CS NPs with good colloidal stability in water and cell culture medium, can effectively discriminate between abnormal and common HOCl cellular physiological concentrations, with an impressive high sensitivity and fast response as a fluorometric turn-off probe with a LOD_{max} of 55 μg mL^{-1}. Moreover, the NPs exhibit an excellent HOCl selectivity over its biological precursors (H_2O_2 and HCl) and other biological reactive oxygen species. MEH NPs exhibit similar behavior, except a higher 83 μg mL^{-1} LOD_{max} value, though these NPs were excluded due to their inability to encapsulate QCT and their limited cellular uptake in both tumoral HeLa cells and RAW264.7 macrophages. Finally, further *in vitro* assays with MEH@CS NPs corroborated the successful intracellular delivery of QCT, inhibiting abnormal endogenous HOCl levels and downregulating concentrations of pro-inflammatory cytokines IL-6 and TNF-α in LPS/PMA-stimulated RAW264.7 cells. In conclusion, QCT-MEH@CS NPs represent a very promising theranostic tool for addressing HOCl-associated inflammatory diseases. Further advantages of this family of NPs when compared with off/on sensors (usually preferred to quenching ones), are: I) the significative fluorescence emission quenching upon HOCl exposure, even at lower analyte concentrations, allows for reliable detection, overcoming challenges related to slight reductions of fluorescence intensity of the sensor; II) the rapid decrease in fluorescence occurs in less than 1 minute, providing a fast detection system; III) third, the emission quenching is associated to the MEH-PPV polymer and NPs degradation, resulting in the release of the payload simply stimulated by the analyte itself; IV) NP intensity remains detectable up to ≈ 50 μM, a value above the physiological range (5–25 μM) enabling early detection of incipient HOCl overproduction and facilitating preventive treatment drug release. This feature is particularly useful for investigating mechanisms associated with intracellular HOCl increments due to inflammatory diseases, such as asthma, rheumatoid arthritis, atherosclerosis and neurodegenerative disorders like Parkinsonś and Alzheimer and last but not least V) it highlights the economic viability of our approach with a rapid and easy manufacturing process.

CRediT authorship contribution statement

Sara Parron-Onate: Visualization, Investigation, Formal analysis, Data curation. **Julia Lorenzo:** Writing – review & editing, Writing – original draft, Resources, Funding acquisition, Conceptualization. **Christian Bellacanzone:** Methodology, Investigation, Formal analysis, Conceptualization. **Aleix Carrascull-Marín:** Investigation, Formal analysis, Data curation. **Olga Wienskowska:** Visualization, Investigation, Formal analysis, Data curation. **Daniel Ruiz-Molina:** Writing – review & editing, Writing – original draft, Supervision, Resources, Project administration, Funding acquisition, Conceptualization. **Claudio Roscini:** Writing – review & editing, Writing – original draft, Supervision, Project administration, Methodology, Funding acquisition, Conceptualization. **Eva Villar-Alvarez:** Writing – review & editing, Writing – original draft, Visualization, Methodology, Investigation, Formal analysis, Data curation, Conceptualization.

Declaration of Competing Interest

The authors declare that they have no known competing financial interests or personal relationships that could have appeared to influence the work reported in this paper.

Data availability

Data will be made available on request.

Acknowledgement

We would like to acknowledge the “Cell cultures, Antibody production and Cytometry Services” of the *Institut de Biotecnologia i de Biomedicina* (IBB) placed associated to the *Universitat Autònoma de Barcelona* (UAB) for their collaboration in cell culture and cytometric assays. E.V.A. acknowledges her *Juan de la Cierva-formación* fellowship FJC2018–036356-I. This work was supported by grants PID2021–127983OB-C21 and PID2021–127983OB-C22 funded by MCIU/AEI/10.13039/501100011033/ and ERDF A way of making Europe, and 2021SGR00135. The ICN2 is funded by the CERCA program/Generalitat de Catalunya and supported by the Severo Ochoa Centres of Excellence programme, Grant CEX2021-001214-S, funded by MCIU/AEI/10.13039.501100011033

Appendix. Supporting Information

Supplementary data associated with this article can be found in the online version at XXX

Appendix A. Supporting information

Supplementary data associated with this article can be found in the online version at doi:10.1016/j.snb.2024.136150.

References

[1] C.M.C. Andrés, J.M. Pérez de la Lastra, C.A. Juan, F.J. Plou, E. Pérez-Lebeña, Hypochlorous acid chemistry in mammalian cells—influence on infection and role in various pathologies, Int. J. Mol. Sci. 23 (2022) e10735, https://doi.org/10.3390/ijms231810735.
[2] W.S. da Cruz Nizer, V. Inkovskiy, J. Overhage, Surviving reactive chlorine stress: responses of gram-negative bacteria to hypochlorous acid, Microorganisms 8 (2020) e1220, https://doi.org/10.3390/microorganisms8081220.
[3] J. Ning, Z. Lin, X. Zhao, B. Zhao, J. Miao, Inhibiting lysine 353 oxidation of GRP78 by a hypochlorous probe targeting endoplasmic reticulum promotes autophagy in cancer cells, Cell Death Dis. 10 (2019) e858, https://doi.org/10.1038/s41419-019-2095-y.
[4] B. Yang, Y. Chen, J. Shi, Reactive oxygen species (ROS)-based nanomedicine, Chem. Rev. 119 (2019) 4881–4985, https://doi.org/10.1021/acs.chemrev.8b00626.
[5] D. Zhang, S. Guo, L. Li, K. Shang, H2O2/HOCl-based fluorescent probes for dynamically monitoring pathophysiological processes, Analyst 145 (2020) 7477–7487, https://doi.org/10.1039/D0AN01313G.
[6] C. Huang, W. Zhou, R. Wu, W. Guan, N. Ye, Recent advances in nanomaterial-based chemiluminescence probes for biosensing and imaging of reactive oxygen species, Nanomaterials 13 (2023) e1726, https://doi.org/10.3390/nano13111726.
[7] R. Zhang, B. Song, J. Yuan, Bioanalytical methods for hypochlorous acid detection: recent advances and challenges, TrAC Trends Anal. Chem. 99 (2018) 1–33, https://doi.org/10.1016/j.trac.2017.11.015.
[8] T. Yudhistira, S.V. Mulay, Y. Kim, M.B. Halle, D.G. Churchill, Imaging of hypochlorous acid by fluorescence and applications in biological systems, Chem. Asian J. 14 (2019) 3048–3084, https://doi.org/10.1002/asia.201900672.

[9] K.H. Kim, S.J. Kim, S. Singha, Y.J. Yang, S.K. Park, K.H. Ahn, Ratiometric detection of hypochlorous acid in brain tissues of neuroinflammation and maternal immune activation models with a deep-red/near-infrared emitting probe, ACS Sens 6 (2021) 3253–3261, https://doi.org/10.1021/acssensors.1c00930.
[10] S. Shao, T. Yang, Y. Han, A TICT-based fluorescent probe for hypochlorous acid and its application to cellular and zebrafish imaging, Sens. Actuators B Chem. 392 (2023) e134041, https://doi.org/10.1016/j.snb.2023.134041.
[11] A.H. Ashoka, F. Ali, R. Tiwari, R. Kumari, S.K. Pramanik, A. Das, Recent advances in fluorescent probes for detection of HOCl and HNO, ACS Omega 5 (2020) 1730–1742, https://doi.org/10.1021/acsomega.9b03420.
[12] H. Li, Y. Miao, Z. Liu, X. Wu, C. Piao, X. Zhou, A mitochondria-targeted fluorescent probe for fast detecting hypochlorite in living cells, Dyes Pigm 176 (2020) e108192, https://doi.org/10.1016/j.dyepig.2020.108192.
[13] J. Han, X. Liu, H. Xiong, J. Wang, B. Wang, X. Song, W. Wang, Investigation of the relationship between H2O2 and HClO in Living Cells by a bifunctional, dual-ratiometric responsive fluorescent probe, Anal. Chem. 92 (2020) 5134–5142, https://doi.org/10.1021/acs.analchem.9b05604.
[14] R. Yadav, K. Odera, A. Rai, R. Takahashi, L. Mishra, Synthesis, characterization, and supramolecular architectures of two distinct classes of probes for the visualization of endogenously generated hypochlorite ions in response to cellular activity, J. Photochem. Photobiol. B 198 (2019) e111594, https://doi.org/10.1016/j.jphotobiol.2019.111594.
[15] X. Song, W. Hu, D. Wang, Z. Mao, Z. Liu, A highly specific and ultrasensitive probe for the imaging of inflammation-induced endogenous hypochlorous acid, Analyst 144 (2019) 3546–3551, https://doi.org/10.1039/C9AN00390H.
[16] J. Zhou, L. Li, W. Shi, X. Gao, X. Li, H. Ma, HOCl can appear in the mitochondria of macrophages during bacterial infection as revealed by a sensitive mitochondrial-targeting fluorescent probe, Chem. Sci. 6 (2015) 4884–4888, https://doi.org/10.1039/C5SC01562F.
[17] C. Jiao, Y. Liu, W. Lu, P. Zhang, X. Ma, Y. Wang, A simple sensor based on 1,8-naphthalimide with large Stokes shift for detection of hypochlorous acid in living cells, RSC Adv. 9 (2019) 31196–31201, https://doi.org/10.1039/C9RA06174F.
[18] J. Gong, C. Liu, S. Cai, S. He, L. Zhao, X. Zeng, Novel near-infrared fluorescent probe with a large Stokes shift for sensing hypochlorous acid in mitochondria, Org. Biomol. Chem. 18 (2020) 7656–7662, https://doi.org/10.1039/D0OB01563F.
[19] D. Shi, S. Chen, B. Dong, Y. Zhang, C. Sheng, T.D. James, Y. Guo, Evaluation of HOCl-generating anticancer agents by an ultrasensitive dual-mode fluorescent probe, Chem. Sci. 10 (2019) 3715–3722, https://doi.org/10.1039/C9SC00180H.
[20] H. Feng, Z. Zhang, Q. Meng, H. Jia, Y. Wang, R. Zhang, Rapid response fluorescence probe enabled in vivo diagnosis and assessing treatment response of hypochlorous acid-mediated rheumatoid arthritis, Adv. Sci. 5 (2018) e1800397, https://doi.org/10.1002/advs.201800397.
[21] M. Ren, K. Zhou, L. He, W. Lin, Mitochondria and lysosome-targetable fluorescent probes for HOCl: recent advances and perspectives, J. Mater. Chem. B 6 (2018) 1716–1733, https://doi.org/10.1039/C7TB03337K.
[22] X.Y. Wong, A. Sena-Torralba, R. Álvarez-Diduk, K. Muthoosamy, A. Merkoçi, Nanomaterials for nanotheranostics: tuning their properties according to disease needs, ACS Nano 14 (2020) 2585–2627, https://doi.org/10.1021/acsnano.9b08133.
[23] H. Liu, P. Zhang, C. Zhang, J. Chen, J.-H. Jiang, Self-assembly of a dual-targeting and self-calibrating ratiometric polymer nanoprobe for accurate hypochlorous acid imaging, ACS Appl. Mater. Interfaces 12 (2020) 45822–45829, https://doi.org/10.1021/acsami.0c13857.
[24] L. Zhang, Y. Xiao, W. Mao, J. Huang, H. Huang, R. Yang, Y. Zhang, X. He, K. Wang, A pyrene-pyridyl nanooligomer as a methoxy-triggered reactive probe for highly specific fluorescence assaying of hypochlorite, Chem. Commun. 58 (2022) 2520–2523, https://doi.org/10.1039/D1CC06606D.
[25] H. Wei, R. Zeng, S. Wang, C.-H. Zhang, S. Chen, P. Zhang, J. Chen, Engineering of a zero cross-talk fluorescent polymer nanoprobe for self-referenced ratiometric imaging of lysosomal hypochlorous acid in living cells, Mater. Chem. Front. 4 (2020) 862–868, https://doi.org/10.1039/C9QM00733D.
[26] K. Wu, C. Yao, D. Yang, D. Liu, A functional DNA nanosensor for highly sensitive and selective imaging of ClO− in atherosclerotic plaques, Biosens. Bioelectron. 209 (2022) e114273, https://doi.org/10.1016/j.bios.2022.114273.
[27] X. Wang, Y. Zuo, Z. Gou, W. Lin, Thiethylated naphthalimide functional silica nanomaterials: a fluorescent nanosensor for detection of HClO in living cells, Dyes Pigm 185 (2021) e108936, https://doi.org/10.1016/j.dyepig.2020.108936.
[28] Y. Cui, J. Wu, J. Zhai, Y. Wang, X. Xie, Spectrally separated dual functional fluorescent nanosensors for subcellular lysosomal detection of hypochlorous acid and chloride, Sens. Diagn. 3 (2024) 319–326, https://doi.org/10.1039/D3SD00275F.
[29] X. Yan, C. Yang, M. Yang, Y. Ma, Y. Zhang, Y. Zhang, C. Liu, Q. Xu, K. Tu, M. Zhang, All-in-one theranostic nano-platform based on polymer nanoparticles for BRET/FRET-initiated bioluminescence imaging and synergistically anti-inflammatory therapy for ulcerative colitis, J. Nanobiotechnol. 20 (2022) e99, https://doi.org/10.1186/s12951-022-01299-8.
[30] B. Ma, H. Xu, W. Zhuang, Y. Wang, G. Li, Y. Wang, Reactive oxygen species responsive theranostic nanoplatform for two-photon aggregation-induced emission imaging and therapy of acute and chronic inflammation, ACS Nano 14 (2020) 5862–5873, https://doi.org/10.1021/acsnano.0c01012.
[31] D. Liu, L. Liu, F. Liu, M. Zhang, P. Wei, T. Yi, HOCl-Activated aggregation of gold nanoparticles for multimodality therapy of tumors, Adv. Sci. 8 (2021) e2100074, https://doi.org/10.1002/advs.202100074.
[32] P. Wei, L. Liu, Y. Wen, G. Zhao, F. Xue, W. Yuan, R. Li, Y. Zhong, M. Zhang, T. Yi, Release of amino- or carboxy-containing compounds triggered by HOCl: application for imaging and drug design, Angew. Chem. Int. Ed. 58 (2019) 4547–4551, https://doi.org/10.1002/anie.201813648.
[33] C. Bellacanzone, C. Roscini, M. del Carmen Ruiz Delgado, R. Ponce Ortiz, D. Ruiz-Molina, Sonochemical synthesis of optically tuneable conjugated polymer nanoparticles, Part. Part. Syst. Charact. 35 (2018) e1700322, https://doi.org/10.1002/ppsc.201700322.
[34] B. Louis, S. Caubergh, P.-O. Larsson, Y. Tian, I.G. Scheblykin, Light and oxygen induce chain scission of conjugated polymers in solution, Phys. Chem. Chem. Phys. 20 (2018) 1829–1837, https://doi.org/10.1039/C7CP07347J.
[35] T.F. Abelha, C.A. Dreiss, M.A. Green, L.A. Dailey, Conjugated polymers as nanoparticle probes for fluorescence and photoacoustic imaging, J. Mater. Chem. B 8 (2020) 592–606, https://doi.org/10.1039/C9TB02582K.
[36] N. Ali, G. Bi, A. Khesro, M. Khan, J. Lang, A. Samreen, H. Wu, Hybrid AgNPs/MEH-PPV nanocomplexes with enhanced optical absorption and photoluminescence properties, N. J. Chem. 42 (2018) 18991–18999, https://doi.org/10.1039/C8NJ04871A.
[37] M. Doshi, A. Copik, A.J. Gesquiere, Development and characterization of conducting polymer nanoparticles for photodynamic therapy in vitro, Photo Photodyn. Ther. 12 (2015) 476–489, https://doi.org/10.1016/j.pdpdt.2015.04.010.
[38] M. Doshi, M. Krienke, S. Khederzadeh, H. Sanchez, A. Copik, J. Oyer, A. J. Gesquiere, Conducting polymer nanoparticles for targeted cancer therapy, RSC Adv. 5 (2015) 37943–37956, https://doi.org/10.1039/C5RA05125H.
[39] C. Szymanski, C. Wu, J. Hooper, M.A. Salazar, A. Perdomo, A. Dukes, J. McNeill, Single Molecule Nanoparticles of the Conjugated Polymer MEH−PPV, Preparation and Characterization by Near-Field Scanning Optical Microscopy, J. Phys. Chem. B 109 (2005) 8543–8546, https://doi.org/10.1021/jp051062k.
[40] M.R. de Oliveira, S.M. Nabavi, N. Braidy, W.N. Setzer, T. Ahmed, S.F. Nabavi, Quercetin and the mitochondria: a mechanistic view, Biotechnol. Adv. 34 (2016) 532–549, https://doi.org/10.1016/j.biotechadv.2015.12.014.
[41] R. Tian, Z. Jin, L. Zhou, X.-P. Zeng, N. Lu, Quercetin attenuated myeloperoxidase-dependent HOCl generation and endothelial dysfunction in diabetic vasculature, J. Agric. Food Chem. 69 (2021) 404–413, https://doi.org/10.1021/acs.jafc.0c06335.
[42] K.T.J. Chen, M. Anantha, A.W.Y. Leung, J.A. Kulkarni, G.G.C. Militao, M. Wehbe, B. Sutherland, P.R. Cullis, M.B. Bally, Characterization of a liposomal copper(II)-quercetin formulation suitable for parenteral use, Drug Deliv. Transl. Res. 10 (2020) 202–215, https://doi.org/10.1007/s13346-019-00674-7.
[43] J. Tang, P. Diao, X. Shu, L. Li, L. Xiong, Quercetin and quercitrin attenuates the inflammatory response and oxidative stress in LPS-Induced RAW264.7 Cells: in vitro assessment and a theoretical model, Biomed. Res. Int. 2019 (2019) 1–8, https://doi.org/10.1155/2019/7039802.
[44] H. Cao, Q. Jia, L. Yan, C. Chen, S. Xing, D. Shen, Quercetin suppresses the progression of atherosclerosis by regulating MST1-mediated autophagy in ox-LDL-Induced RAW264.7 macrophage foam cells, Int. J. Mol. Sci. 20 (2019) e6093, https://doi.org/10.3390/ijms20236093.
[45] M.K. Lawson, Improvement of therapeutic value of quercetin with chitosan nanoparticle delivery systems and potential applications, Int. J. Mol. Sci. 24 (2023) e3293, https://doi.org/10.3390/ijms24043293.
[46] J. Zhou, N. Li, P. Liu, Z. Liu, L. Gao, T. Jiao, Preparation of fluorescently labeled chitosan-quercetin drug-loaded nanoparticles with excellent antibacterial properties, J. Funct. Biomater. 13 (2022) e141, https://doi.org/10.3390/jfb13030141.
[47] C. Moraru, M. Mincea, G. Menghiu, V. Ostafe, Understanding the factors influencing chitosan-based nanoparticles-protein corona interaction and drug delivery applications, Molecules 25 (2020) e4758, https://doi.org/10.3390/molecules25204758.
[48] R. Safdar, A.A. Omar, A. Arunagiri, I. Regupathi, M. Thanabalan, Potential of chitosan and its derivatives for controlled drug release applications – a review, J. Drug Deliv. Sci. Technol. 49 (2019) 642–659, https://doi.org/10.1016/j.jddst.2018.10.020.
[49] E. Villar-Alvarez, B.H. Leal, R. Martínez-González, A. Pardo, S. Al-Qadi, J. Juárez, M.A. Váldez, A. Cambón, S. Barbosa, P. Taboada, siRNA Silencing by chemically modified biopolymeric nanovectors, ACS Omega 4 (2019) 3904–3921, https://doi.org/10.1021/acsomega.8b02875.
[50] M. Kara, O.F. Beser, D. Konukoglu, H. Cokugras, T. Erkan, T. Kutlu, F.C. Cokugras, The utility of TNF-α, IL-6 and IL-10 in the diagnosis and/or follow-up food allergy, Allergol. Immunopathol. (Madr. 48 (2020) 48–55, https://doi.org/10.1016/j.aller.2019.04.011.
[51] S. Kany, J.T. Vollrath, B. Relja, Cytokines in inflammatory disease, Int. J. Mol. Sci. 20 (2019) e6008, https://doi.org/10.3390/ijms20236008.
[52] M.D. Turner, B. Nedjai, T. Hurst, D.J. Pennington, Cytokines and chemokines: at the crossroads of cell signalling and inflammatory disease, Biochim. Biophys. Acta Mol. Cell Res. 1843 (2014) 2563–2582, https://doi.org/10.1016/j.bbamcr.2014.05.014.
[53] I. Peluso, A. Raguzzini, M. Serafini, Effect of flavonoids on circulating levels of TNF-α and IL-6 in humans: a systematic review and meta-analysis, Mol. Nutr. Food Res. 57 (2013) 784–801, https://doi.org/10.1002/mnfr.201200721.
[54] J. Huang, Y. Qin, B. Liu, G.Y. Li, L. Ouyang, J.H. Wang, In silico analysis and experimental validation of molecular mechanisms of salvianolic acid A-inhibited LPS-stimulated inflammation, in RAW264.7 macrophages, Cell Prolif. 46 (2013) 595–605, https://doi.org/10.1111/cpr.12056.
[55] J.V. Morris, M.A. Mahaney, J.R. Huber, Fluorescence quantum yield determinations. 9,10-Diphenylanthracene as a reference standard in different solvents, J. Phys. Chem. 80 (1976) 969–974, https://doi.org/10.1021/j100550a010.

[56] H.ölzl-Armstrong Kucab, Korenjak Luijten, Phillips Zavadil, Arlt, Characterising mutational spectra of carcinogens in the tumour suppressor gene TP53 using human TP53 knock-in (Hupki) mouse embryo fibroblasts, Methods Protoc. 2 (2019) e85, https://doi.org/10.3390/mps2040085.
[57] J. Crecente-Campo, M.J. Alonso, Engineering, on-demand manufacturing, and scaling-up of polymeric nanocapsules, Bioeng. Transl. Med. 4 (2019) 38–50, https://doi.org/10.1002/btm2.10118.
[58] P. Das, A. Kumar, A. Chowdhury, P.S. Mukherjee, Aggregation-induced emission and white luminescence from a combination of π-conjugated donor–acceptor organic luminogens, ACS Omega 3 (2018) 13757–13771, https://doi.org/10.1021/acsomega.8b01706.
[59] C. Galey, H. Park, Intermediate states during photodegradation in MEH-PPV solutions and thin films, AIP Adv. 9 (2019) e105010, https://doi.org/10.1063/1.5099382.
[60] D. Bondarev, O. Trhlíková, J. Sedláček, J. Vohlídal, Stability of MEH-PPV: Poly{[2-methoxy-5-(2-ethylhexyloxy)-1,4-phenylene]vinylene} in solutions exposed to air in the dark and at daylight at laboratory temperature, Polym. Degrad. Stab. 110 (2014) 129–136, https://doi.org/10.1016/j.polymdegradstab.2014.08.015.
[61] T.L. Moore, L. Rodriguez-Lorenzo, V. Hirsch, S. Balog, D. Urban, C. Jud, B. Rothen-Rutishauser, M. Lattuada, A. Petri-Fink, Nanoparticle colloidal stability in cell culture media and impact on cellular interactions, Chem. Soc. Rev. 44 (2015) 6287–6305, https://doi.org/10.1039/C4CS00487F.
[62] D. Perrin, Buffers of low ionic strength for spectrophotometric pK determinations, Aust. J. Chem. 16 (1963) 572–578, https://doi.org/10.1071/CH9630572.
[63] F. Barbero, L. Russo, M. Vitali, J. Piella, I. Salvo, M.L. Borrajo, M. Busquets-Fité, R. Grandori, N.G. Bastús, E. Casals, V. Puntes, Formation of the protein corona: the interface between nanoparticles and the immune system, Semin. Immunol. 34 (2017) 52–60, https://doi.org/10.1016/j.smim.2017.10.001.
[64] R. Rampado, S. Crotti, P. Caliceti, S. Pucciarelli, M. Agostini, Recent advances in understanding the protein corona of nanoparticles and in the formulation of "stealthy" nanomaterials, Front. Bioeng. Biotechnol. 8 (2020) e166, https://doi.org/10.3389/fbioe.2020.00166.
[65] H. Shin, M. Kwak, T.G. Lee, J.Y. Lee, Quantifying the level of nanoparticle uptake in mammalian cells using flow cytometry, Nanoscale 12 (2020) 15743–15751, https://doi.org/10.1039/D0NR01627F.
[66] G. Sanità, B. Carrese, A. Lamberti, Nanoparticle surface functionalization: how to improve biocompatibility and cellular internalization, Front. Mol. Biosci. 7 (2020) e587012, https://doi.org/10.3389/fmolb.2020.587012.
[67] P. Foroozandeh, A.A. Aziz, Insight into cellular uptake and intracellular trafficking of nanoparticles, Nanoscale Res. Lett. 13 (2018) e339, https://doi.org/10.1186/s11671-018-2728-6.
[68] J. Zhao, M.H. Stenzel, Entry of nanoparticles into cells: the importance of nanoparticle properties, Polym. Chem. 9 (2018) 259–272, https://doi.org/10.1039/C7PY01603D.
[69] Z. Chen, L. Zhang, Y. Song, J. He, L. Wu, C. Zhao, Y. Xiao, W. Li, B. Cai, H. Cheng, W. Li, Hierarchical targeted hepatocyte mitochondrial multifunctional chitosan nanoparticles for anticancer drug delivery, Biomaterials 52 (2015) 240–250, https://doi.org/10.1016/j.biomaterials.2015.02.001.
[70] A.A. Zubareva, T.S. Shcherbinina, V.P. Varlamov, E.V. Svirshchevskaya, Intracellular sorting of differently charged chitosan derivatives and chitosan-based nanoparticles, Nanoscale 7 (2015) 7942–7952, https://doi.org/10.1039/C5NR00327J.
[71] H. Wang, B. Fang, B. Peng, L. Wang, Y. Xue, H. Bai, S. Lu, N.H. Voelcker, L. Li, L. Fu, W. Huang, Recent advances in chemical biology of mitochondria targeting, Front. Chem. 9 (2021) e683220, https://doi.org/10.3389/fchem.2021.683220.
[72] N. Aibani, R. Rai, P. Patel, G. Cuddihy, E.K. Wasan, Chitosan nanoparticles at the biological interface: implications for drug delivery, Pharmaceutics 13 (2021) e1686, https://doi.org/10.3390/pharmaceutics13101686.
[73] Q. Li, Y. Huang, Mitochondrial targeted strategies and their application for cancer and other diseases treatment, J. Pharm. Investig. 50 (2020) 271–293, https://doi.org/10.1007/s40005-020-00481-0.
[74] L. Fang, H. Lin, Z. Wu, Z. Wang, X. Fan, Z. Cheng, X. Hou, D. Chen, In vitro/vivo evaluation of novel mitochondrial targeting charge-reversal polysaccharide-based antitumor nanoparticle, Carbohydr. Polym. 234 (2020) e115930, https://doi.org/10.1016/j.carbpol.2020.115930.
[75] Y. Tan, Y. Zhu, L. Wen, X. Yang, X. Liu, T. Meng, S. Dai, Y. Ping, H. Yuan, F. Hu, Mitochondria-responsive drug release along with heat shock mediated by multifunctional glycolipid micelles for precise cancer chemo-phototherapy, Theranostics 9 (2019) 691–707, https://doi.org/10.7150/thno.31022.
[76] S. Marrache, S. Dhar, Engineering of blended nanoparticle platform for delivery of mitochondria-acting therapeutics, Proc. Nat. Acad. Sci. 109 (2012) 16288–16293, https://doi.org/10.1073/pnas.1210096109.
[77] R.K. Pathak, N. Kolishetti, S. Dhar, Targeted nanoparticles in mitochondrial medicine, WIREs Nanomed. Nanobiotechnol. 7 (2015) 315–329, https://doi.org/10.1002/wnan.1305.
[78] D. Abbaszadeh, A. Kunz, N.B. Kotadiya, A. Mondal, D. Andrienko, J.J. Michels, G.-J.A.H. Wetzelaer, P.W.M. Blom, Electron trapping in conjugated polymers, Chem. Mater. 31 (2019) 6380–6386, https://doi.org/10.1021/acs.chemmater.9b01211.
[79] F. Allegrini, A.C. Olivieri, IUPAC-Consistent approach to the limit of detection in partial least-squares calibration, Anal. Chem. 86 (2014) 7858–7866, https://doi.org/10.1021/ac501786u.
[80] H. Evard, A. Kruve, I. Leito, Tutorial on estimating the limit of detection using LC-MS analysis, part I: theoretical review, Anal. Chim. Acta 942 (2016) 23–39, https://doi.org/10.1016/j.aca.2016.08.043.
[81] L.U. Syed, L.Z. Swisher, H. Huff, C. Rochford, F. Wang, J. Liu, J. Wu, M. Richter, S. Balivada, D. Troyer, J. Li, Luminol-labeled gold nanoparticles for ultrasensitive chemiluminescence-based chemical analyses, Analyst 138 (2013) 5600–5609, https://doi.org/10.1039/c3an01005h.
[82] W.M.T. Kuwabara, L. Zhang, I. Schuiki, R. Curi, A. Volchuk, T.C. Alba-Loureiro, NADPH Oxidase-dependent production of reactive oxygen species induces endoplasmatic reticulum stress in neutrophil-like HL60 cells, PLoS One 10 (2015) e0116410, https://doi.org/10.1371/journal.pone.0116410.
[83] W. Gao, Y. Liu, H. Zhang, Z. Wang, Electrochemiluminescence biosensor for nucleolin imaging in a single tumor cell combined with synergetic therapy of tumor, ACS Sens 5 (2020) 1216–1222, https://doi.org/10.1021/acssensors.0c00292.
[84] L. George, T. Ramasamy, K. Sirajudeen, V. Manickam, LPS-induced apoptosis is partially mediated by hydrogen sulphide in RAW 264.7 murine macrophages, Immunol. Invest. 48 (2019) 451–465, https://doi.org/10.1080/08820139.2019.1566355.
[85] P. Klitou, I. Rosbottom, V. Karde, J.Y.Y. Heng, E. Simone, Relating crystal structure to surface properties: a study on quercetin solid forms, Cryst. Growth Des. 22 (2022) 6103–6113, https://doi.org/10.1021/acs.cgd.2c00707.
[86] L. Cao, H. Feng, F. Meng, J. Li, L. Wang, Fabrication of a high tensile and antioxidative film via a green strategy of self-growing needle-like quercetin crystals in cassia gum for lipid preservation, J. Clean. Prod. 266 (2020) e121885, https://doi.org/10.1016/j.jclepro.2020.121885.
[87] A. Bardestani, S. Ebrahimpour, A. Esmaeili, A. Esmaeili, Quercetin attenuates neurotoxicity induced by iron oxide nanoparticles, J. Nanobiotechnol. 19 (2021) e327, https://doi.org/10.1186/s12951-021-01059-0.
[88] P. Klitou, E. Parisi, S. Bordignon, F. Bravetti, I. Rosbottom, M. Dell'Aera, C. Cuocci, M.R. Chierotti, A. Altomare, E. Simone, Navigating the complex solid form landscape of the quercetin flavonoid molecule, Cryst. Growth Des. 23 (2023) 6034–6045, https://doi.org/10.1021/acs.cgd.3c00584.
[89] A.G. Veiko, E.A. Lapshina, I.B. Zavodnik, Comparative analysis of molecular properties and reactions with oxidants for quercetin, catechin, and naringenin, Mol. Cell Biochem. 476 (2021) 4287–4299, https://doi.org/10.1007/s11010-021-04243-w.
[90] P. Sahoo, P. Jana, S. Kundu, S. Mishra, K. Chattopadhyay, A. Mukherjee, C. K. Ghosh, Quercetin@Gd3+ doped Prussian blue nanocubes induce the pyroptotic death of MDA-MB-231 cells: combinational targeted multimodal therapy, dual modal MRI, intuitive modelling of r1- r2 relaxivities, J. Mater. Chem. B 11 (2023) 6646–6663, https://doi.org/10.1039/D3TB00316G.
[91] P. Klitou, I. Rosbottom, V. Karde, J.Y.Y. Heng, E. Simone, Relating crystal structure to surface properties: a study on quercetin solid forms, Cryst. Growth Des. 22 (2022) 6103–6113, https://doi.org/10.1021/acs.cgd.2c00707.
[92] P. Klitou, I. Rosbottom, E. Simone, Synthonic modeling of quercetin and its hydrates: explaining crystallization behavior in terms of molecular conformation and crystal packing, Cryst. Growth Des. 19 (2019) 4774–4783, https://doi.org/10.1021/acs.cgd.9b00650.
[93] H. Moon, P. Lertpatipanpong, Y. Hong, C.-T. Kim, S.J. Baek, Nano-encapsulated quercetin by soluble soybean polysaccharide/chitosan enhances anti-cancer, anti-inflammation, and anti-oxidant activities, J. Funct. Foods 87 (2021) e104756, https://doi.org/10.1016/j.jff.2021.104756.
[94] Z. Yarjanli, K. Ghaedi, A. Esmaeili, A. Zarrabi, S. Rahgozar, The antitoxic effects of quercetin and quercetin-conjugated iron oxide nanoparticles (QNPs) against H2O2-induced toxicity in PC12 cells, Int. J. Nanomed. 14 (2019) 6813–6830, https://doi.org/10.2147/IJN.S212582.
[95] J. Peng, Z. Yang, H. Li, B. Hao, D. Cui, R. Shang, Y. Lv, Y. Liu, W. Pu, H. Zhang, J. He, X. Wang, S. Wang, Quercetin reprograms immunometabolism of macrophages Via the Sirt1/pgc-1α signaling pathway to ameliorate lipopolysaccharide-induced oxidative damage, Int. J. Mol. Sci. 24 (2023) e5542, https://doi.org/10.3390/ijms24065542.

Daniel Ruiz-Molina earned his PhD in polyradical dendrimers at the Institut de Ciència de Materials de Barcelona (ICMAB-CSIC) under Prof. Jaume Veciana. He then took a postdoctoral position at the University of California San Diego (USA), where he spent three years working on single molecule magnets and molecular switches. Since 2001 he has held a permanent position as a Spanish National Research Council (CSIC) researcher, most recently at the ICN2, where he is the leader of the ICN2 Nanostructured Functional Materials Group also known as NanosFun. His main research areas include the fabrication of hybrid colloids and surfaces, biomimetic functional nanostructures, and micro- or nanoparticles for smart applications and encapsulation and delivery systems. H-index: 41 (Google Scholar)